A review of recent trends in polymer characterization using non-destructive vibrational spectroscopic modalities and chemical imaging

Article *in* Analytica Chimica Acta · September 2015

Impact Factor: 4.51 · DOI: 10.1016/j.aca.2015.09.006

2 authors:

Sindhuraj Mukherjee
University College Dublin
1 PUBLICATION **1** CITATION
SEE PROFILE

Aoife Gowen
University College Dublin
80 PUBLICATIONS **1,292** CITATIONS
SEE PROFILE

A review of recent trends in polymer characterization using non-destructive vibrational spectroscopic modalities and chemical imaging.

Sindhuraj Mukherjee, Aoife Gowen**

*School of Biosystems Engineering, University College Dublin, Belfield, Dublin 4, Co. Dublin, Ireland

KEYWORDS Chemical imaging, polymer, hyperspectral imaging, chemometrics, spectroscopy, application, biomaterial

ABSTRACT This review focuses on the recent developments in vibrational spectroscopy andchemical imaging (i.e. Raman, Near Infrared, Mid Infrared) to characterize polymers in diverse forms, their behaviour and transient phenomenon. First, important polymeric properties and traditional methods of their characterization are outlined. Then relative advantages & disadvantages have been presented of different characterization methods are presented. This is followed by a detailed review of applications of chemical imaging and spectroscopic techniques in polymer characterization, including the limitations encountered. The article ends with a discussion on the future of chemical imaging with regards to polymer characterization.

Keywords : Polymer characterization; Chemical imaging; Hyperspectral Imaging; Chemometrics; Spatial imaging; Multivariate analysis

List of tables
Table 1 Traditional methods of polymer characterization
Table 2 Peak annotation for vibrational and rotational frequencies of chemical species from Infrared & Raman spectra
Table 3 Table outlining major Infrared and Raman modalities compared in this review
Table 4 Table listing the advantages and disadvantages of different techniques
Table 5 Table summarising all the non-spatial and spatial analyses covered in this review paper

List of figures
Figure 1: The image shows the reflectance based blend distribution image of a PLLA: P3HB 50:50 blend solvent cast film. Yellow/Red sections show the concentration of Poly-L-Lactic acid(PLLA) and the green/blue section shows concentrations of Poly-3-hydroxybutyrate(P3HB) by selecting the 1753cm^{-1} representing the C=O bond(PLLA) and 1720cm^{-1} for the same bond (P3HB) in the blend. This image was taken using air as reference, 4000-800 cm^{-1}range, spectral resolution = 4 cm^{-1}, spatial resolution = 4um
Figure 2 : Application of Principal Component Analysis(PCA) to a chemical image. First the data cube is unfolded. PCA is applied to the unfolded data cube resulting in scores, loadings and a residual matrix. λ = wavelength range of the spectral component ($\lambda_1 \ldots \lambda_n$), X and Y refer to the indices for spatial components, spanning the image scan area. (X,Y,λcan have values ranging from 1 to n, which are pixel indices for the image).
Figure 3 :A chemical image of a polymer blend (PLLA:PHB, 50:50) was subjected to PCA. PC score images (1-5, >99% variance in dataset) were used as inputs to a Gaussian mixture clustering algorithm, with 2 classes. The results of this are shown in the middle section of Fig 3, where black pixels represent Class 1 and white pixels represent Class 2. The class membership (i.e. the posterior probability of a pixel belonging to each class) is shown on the right hand side of Figure 3. This kind of soft classification can be used to identify intermediate pixels belonging to both classes.
Figure 4 : Image representing the 1634cm^{-1} band intensity of lubricant in a polyurethane matrix taken using AFM-IR. Image sourced from [1]
Figure 5 : Infrared nano-imaging of a polymer thin film (PMMA) on a Si substrate. [2]

Figure 6 :FTIR image of non-degrading PLLA/HA composite material (a) FTIR image based on the absorption band at 1755cm-1; (b) color scale; and (c) FTIR spectra of different pixels in the image. Image sourced from [3]

Figure 7 : Orange represents the SWCNT : G-band distribution (black represents high concentration of SWCNT), white represents the epoxy resin distribution. Image sourced from [4]

Figure 8 : From left to right, predicted crystallinity values of HDPE, LDPE & PP. Predicted crystallinity distribution for HDPE cooled at 4 C/min. Values are given in % crystallinity. Sample size: 100 mm×40 mm. Method 1 uses averaged NIR spectra & PLS regression, Method 2 uses second derivative NIR spectra & PLS regression, Method 3 uses MIA/MIR using raw reflectance spectra, Method 4 uses MIA/MIR using second derivative spectra. Image sourced from [5]

Figure 9 : Optical image of PLLA sample (left), SNV treated spectra of predicted crystallinity of same section (right). PLLA sample kept on hot stage, depict the effect of temperature and crystallinity on the top portion of the image. Image sourced from [6]

Figure 10 :CARS hyperspectral image of the PS/PP blend. The raw CARS data was used to construct animage(left), where the red and blue color indicates the intensity at 990 and 2880 cm^{-1}, respectively for polystyrene(PS) and polypropylene(PP). Image sourced from [7]

Figure 11 : Chemically selective imaging is demonstrated for composite material of polypropylene (PP) matrix and om-POSS (octamethyl polyhedral oligomericsilsesquioxane) microparticles having partly overlapping CH stretching vibrations.CARS images measured at a probe delay of (A) 0.10 ps and (B) 0.48 ps and (C) image obtained by dividing the CARS intensity at each pixel at 0.48 ps by the intensity at 0.10 ps. (D−F) Profiles of CARS intensities across images A−C, respectively. Image sourced from [8]

Figure 12 : This figure shows the distribution of different components as predicted by the PLS-DA model. Pure drug theophylline is represented by black, whose distribution can be visualised in the middle picture. Image sourced from [9]

Figure 13 : Concentration maps of HPMC, PVP, PEG and PAR obtained from PLS models. Image sourced from [3]

Figure 14 : Figure 14 shows the score images of indomethacin inclusion into polymer networks $PHEMA_{PVA}$ (a); $PHEMA_{PAS}$ (b); and $PHEMA_{CD}$. Image sourced from [4]. Level of grey depicts the distribution of the indomethacin in the synthesized polymeric matrices. Image sourced from [10]

Figure 15 :AFM and AFM-IR chemical images of water within Nafion film, (a) AFM topography, (b) free water at 3482 cm−1 (c) bound water at 3211 cm−1, and (d) AFM-IR spectra at point C1 and C2. Images (a) and (b) show that free water and bound water are distributed differently on the Nafion

membrane surface. Image sourced from [11]

1. INTRODUCTION

In order to tailor polymers to different applications e.g. thin films for packaging, coatings for drugs, scaffolds for biomedical engineering, it is necessary to conduct a thorough study of their physico-chemical properties such as molecular mass, structure, morphology, thermal characteristics, and mechanical characteristics. Synthetic polymers are commonly created in different forms such as pellets, composites, blends, films, colloids, coatings. Therefore,

instrumental techniques capable of accurate, reliable and rapid evaluation of polymers are required. Traditional methods for polymer characterization (summarized in **Table 1**) typically involve laborious sample preparation, are time consuming, destructive in nature and/or invasive, all of which may lead to loss of crucial information of polymer in its *natural state*. Therefore, there is a need for technologies which bypass above mentioned shortcomings and allow for a prediction based approach for characterization with minimum loss of information.

----------TABLE 1 goes here----------

1.1 Vibrational spectroscopy

Vibrational spectroscopy is a well-established area of applied spectroscopy that enables molecular characterization of materials based on the vibrations of atoms and molecules[1][2][3][4][5][6]. Infrared & Raman spectroscopy are the most widespread vibrational spectroscopic modalities in common use[7][8][9]. When infrared radiation passes through a sample, bonds between atoms vibrate due to absorption of energy Different molecules and functional groups exhibit characteristic absorption peaks corresponding to the frequency of a vibration in a given molecule[10][11]. Based on the range of frequencies studied, infrared spectroscopy is subdivided into three categories: the near infrared (NIR) region within the 400nm-2500nm or 25000-4000cm^{-1} range, which is sensitive to overtone and combinations of

vibrational vibrations; the mid infrared (MIR) region within the 2500nm-25000nm or 4000-400cm^{-1} range to study fundamental vibrations and the far infrared (FIR) region spanning 25000-1000000nm or 400-10cm^{-1} range to study rotations.

MIR spectra are typically obtained using interferometer based Fourier Transfrom Infrared (FTIR) systems. For samples thicker than a few 100um, a large amount of IR energy absorbed by the sample results in a low signal to noise spectrum. This can be overcome by the use of Attenuated Total Reflection (ATR), where a polished crystal surface(e.g., diamond, germanium) contacts the sample surface, IR light passes through the crystal, generates an evanescent wave through the sample[12].

The penetration depth of analysis in ATR-FTIR is generally between 0.5-5um, as the following equation shows :[13]

$$\mathrm{Dp} = \frac{\lambda}{\left\{2\pi n_1 \left[\sin^2\theta - \left(\frac{n_2}{n_1}\right)^2\right]^{0.5}\right\}}$$

Where D_p= depth of penetration, n_1 , n_2 are refractive indices of prism and sample respectively, θ is the angle of incidence of the infrared light, and λ is the wavelength of light.

In Raman spectroscopy, a laser irradiates the sample, causing a distortion in the electron cloud around molecules in the sample. This distortion is the result of an inelastic scattering of a photon by the molecule, causing the photon to gain from (blue shift) or lose energy to the molecule (red shift)[14]. A plot of the scattered intensity versus the energy difference between incident and scattered photons gives the Raman spectrum.

Identification of peaks in an IR or Raman spectrum corresponding to different functional groups is usually achieved by a series of calculations based on the degrees of freedom and quantum dynamics of the molecule[15]. These calculations are only predictive, and peak position may vary due to the experimental setup, chemical preparation and sample matrix. Therefore, one must exercise caution in peak assignment.

Peak locations for functional groups in a variety of polymers are listed in **Table 2**. Commercially available polymer libraries, which are built using polymer based standards, enable rapid identification/estimation of composition

----------TABLE 2 goes here----------

Vibrational spectroscopic analysis I suited to the study of most solids and liquid polymeric samples. However, when the homogeneity of polymeric properties throughout a sample is of interest vibrational point spectroscopy is somewhat limited [9] because the spatial variation of these properties is not measured.

1.2 Chemical imaging

Recent developments in the field of digital imaging allow spatially resolved spectroscopic information to be captured from polymers, rapidly and non-destructively. Spatially resolved vibrational spectroscopic techniques, generally referred to as 'chemical imaging' or 'hyperspectral imaging' allow us to generate 'chemical maps' from data rich information structures called 'data cubes where each pixel in an image contains a spectrum ; For example, in Figure 1, an ATR-

FTIR chemical map of a based on the carbonyl stretching band of C=O stretch at 1740cm^{-1} is shown. Mathematically, these data cubes can be thought of as a 3 dimensional data set, A(x,y,z), where x,y are spatial coordinates and z is the spectral coordinate.

----------FIGURE 1 goes here ----------

As chemical imaging evolved, different instrument configurations were developed to allow a wide variety of analysis (wavelength range, type of detector, data acquisition mode, acquisition time, light source). They can be grouped as infrared imaging (FTIR, ATR-FTIR, synchrotron FTIR, AFM-IR, s-SNOM) and Raman imaging (CRM, TERM, B-CARS, TR-CARS) techniques. In **Table 3**, a short description of each of these techniques is provided, and further information can be found in the references provided.

----------TABLE 3 goes here----------

Each of the chemical imaging techniques mentioned in **Table 3**, have advantages and disadvantages as listed in **Table 4**. An appropriate understanding of scenarios where a specific technique can provide more relevant information is important for the investigator.

----------TABLE 4goes here ----------

1.3 Data Processing &Chemometrics

In order to identify specific chemical constituents in a polymer and to study changes to the bonds, one initially takes a univariate approach, i.e., using one or two bands linked to specific chemical bonds present in the polymer. Changes occurring due to natural or synthetic processing

steps that affect the polymer would be reflected by a change in the band intensity, area or location of the peak. Based on this assumption, spectral analysis can be linked to conventional methods of polymer analysis such as DSC. However, this approach depends on prior knowledge of exclusive bands related to polymers, which may not properly represent a dynamic chemical system (often the interest of systems engineers) and this is the rationale for the introduction of multivariate analysis techniques or chemometrics.

Moreover, data cubes are data rich and their analysis is challenging. To make sense of the 3 dimensional data sets (time domain studies include an additional time dimension‘t’) and gain meaningful information, the discipline of chemometrics is useful. Chemometric methods utilise mathematical and statistical techniquesin which to identify relevant trends in data. Trends analysed using chemometrics can be connected to conventional methods of polymer physicochemical characterization, in order to model and predict properties of interest. The most common chemometric qualitative and quantitative approaches encountered in chemical imaging are described below.

Before beginning chemometric analyses, it is important to note that, the data cubes often suffer from problems related to signal capture, which can be circumvented using data pre-processing. Common data pre-processing techniques include application of local filters for dead pixel removal, spike removal, background estimation-removal, baseline correction and applications of derivatives. Further pre-processing of spectra includes methods such as multiplicative scatter correction, normalisation and mean-centring.[16]. Once relevant data pre-processing is applied to the data cube, it becomes pertinent for the researcher to explore the data cube and analyse it for trends, in other words to begin chemometric analyses. Chemometrics analysis typically begins

with the exploration of data using qualitative methods. Qualitative chemometric methods are used in order to search for groups within the data cube. These include Principal Component Analysis (PCA) and some clustering techniques (e.g. k-means, c-means, hierarchical or tree based clustering,).Quantitative methods include multivariate curve resolution-regression (MCR-ALS) , partial least square regression (PLSR), classical least square-regression (CLSR), and multivariate linear regression and artificial neural networks[16].

In PCA, a captured and pre-processed hyperspectral image is first unfolded into a 2-dimensional matrix X, containing pixel intensity values at each wavelength. X is then decomposed into scores (T) and loadings (P) as shown in the equation below(this can be visualized in **Fig 2**). Each principal component is a linear combination of the original wavelength variables, combined in such a way that the first principal component captures the majority of variability in the original data matrix X, the second PC is orthogonal to the first and contains the next greatest variability, and so on.

$$X_{(i,j,k)} = T_A \,.\, P_A^T + E_{(i,j,k)}$$

where A is the number of principal components, underlying structures or 'chemical' rank of the matrix ; the score vectors, T = [t_1, t_2, …. t_A], give the coordinates of samples in the PC space, hence score scatter plots allow the inspection of sample similarity/dissimilarity.The loading vectors, P = [p_1,p_2, …. p_A], represent the weight with which each original variable contributes to the principal components; E is the residual or noise or error matrix, the part of the data unexplained, and can be used to identify outliers and variables as visualised in Figure 2. [16]

----------FIGURE 2 GOES HERE, unfolding, PCA----------

.

Data clustering techniques cover a major area of hyperspectral data analysis and broadly speaking, refer to the application of mathematical constraints on spectral data points to find groups or clusters of similar data points [16]. In spectroscopic analysis, one can use similarity or dissimilarity of spectra as the mathematical basis for clustering. Clustering techniques can be divided into hard clustering or soft clustering techniques based on the strength of mathematical constraint applied.

----------FIGURE 3 goes here-clustering----------

In hard clustering (e.g. K-means clustering), a given data point can only belong to one cluster. In contrast, in case of soft clustering (eg.Fuzzyc-means), a given sample (i.e. pixel spectrum) can belong to more than one class. The distinction between soft and hard clustering methods is shown in Figure 3. A chemical image of a polymer blend (PLLA:PHB, 50:50) was first subjected to PCA to reduce the dimensionality of the dataset prior to cluster analysis. PC score images (PC 1-5, representing >99% variance in dataset) were used as inputs to a Gaussian mixture clustering algorithm, with 2 target classes. The results of this are shown in the middle section of Fig 3, where black pixels represent class 1 and white pixels represent class 2. The class membership (i.e. the posterior probability of a pixel belonging to each class) is shown on the right hand side of Figure 3. Gray pixels represent the pixels belonging to both classes.

For quantitative analysis, Partial Least Squares Regression (PLSR), can be used to establish relationships between spectra and measured variables (e.g. blend ratios or concentrations of

known components) to create predictive models[16]. In PLSR, a reference data set consisting of spectra with known analyte concentrations is used to build a calibration model for these analytes. Instead of looking for the variance in the spectra (as in PCA), the co-variance between the constituent concentrations and the spectra is used [17]. The following section is a comprehensive review of recent applications of CI to polymer characterization as summarized in **Table 5**.

----------TABLE 5 goes here ----------

2. Applications of chemical imaging in polymer characterization

2.1 COATING

In this section, the application of chemical imaging techniques to investigate the presence of polymeric layers on other polymers or substrates, determination of layer thickness as well as their degradation under specific environments are discussed. Relevant chemometric techniques and a comparison of non-spatial or point spectroscopic techniques and spatial analysis are provided.

2.1.1 Coating characterization

The design and development of polymer based materials for implantation in humans requires careful consideration of biocompatibility and surface interactions. For example, the development of hollow fibre membranes as artificial lungs requires a large surface area of blood contact to allow sufficient gas exchange. In a recent study by Wang et al[18] a biomimetic coating poly (2-methacryloyloxyethyl phosphorylcholine-co-n-butyl methacrylate- co-3-(Tri-methoxysilyl) propyl methacrylate) or PMBT, was polymerized by dip coating on polypropylene hollow fibre

membranes to improve hemocompatibility. This coating mimics the outer layer of a red blood cell and allows greater gaseous exchange as opposed to hollow fibre membranes made of polypropylene and polysulfone, which aremore common. ATR-FTIR spectroscopy was used to confirm copolymer film formation on the membranes. Spectra were obtained, for coated and uncoated membranes and spectral peaks corresponding to C=O (1750 cm^{-1} stretch vibration) and O-P=O (1240 and 1080 cm^{-1}, asymmetric and symmetric stretch), characteristic of 2-methacryloyloxyethyl phosphorylcholine, were selected and compared to confirm the presence of the coating. In this case, the selection of the 3 mentioned bands for detecting the coating was sufficient when compared parallel to XPS. Scanning electron microscopy revealed some differences between the bare and PMBT coated membranes in terms of the number and size of the pores on the surface, which are not possible to visualize with point spectroscopy. However, the uniformity of coating thickness was not explored. The use of FTIR or Raman imaging could provide additional information on the spatial distribution of the coating on such surfaces.

Dazzi et al [1] investigated the use of Atomic Force Microscopy Infrared Imaging (AFM-IR) to visualise the distribution of a lubricant, ethylene bisstearamide (EBS) on a silicon wafer spin coated with polyether-urethane(thickness 1-2µm). The absorptions at 1634 cm^{-1} (νC = O) and 1560 cm^{-1} (νC–N + δN–H) characteristic of the amide bands of the ethylene bisstereamide(EBS), were used to generate chemical maps visualising the distribution of the lubricant deposits.

----------INSERT FIGURE 4 here----------

This ability to spatially resolve features at the nanometre scale, and provide spectroscopic identification is the biggest advantage of using AFM-IR. This is significant when compared to a

technique such as XPS, which can detect such deposits, but cannot give any spatial distribution information.

Another recent advancement in obtaining highly spatially resolved chemical images at the nanometre scale has been achieved by using a scattering-type scanning near-field optical microscope (s-SNOM) equipped with a coherent-continuum infrared light source. Huth et al [2] imaged a silicon wafer (polydimethylsiloxane or PDMS) coated with poly- (methyl methacrylate) (PMMA) (thickness 90nm) using s-SNOM in the 2100-700 cm^{-1} range, over a 1 μm x 1 μm scan area, at a spectral resolution of 13 cm^{-1} and a spatial resolution of 20nm (characteristic of the gold AFM tip used). PMMA was easily identified using the 1730cm (C=O stretching), 1265 cm−1 and 1240 cm−1 (C−C−O stretching), 1190 cm−1 (C−O−C bending), and 1145 cm−1 (CH_2 bending).

----------INSERT FIGURE5 here----------

A scratch made on the surface of this coating, was also imaged, and PDMS related bands at 1260 cm^{-1} (Si-CH_3 symmetric deformation) and 1100 cm^{-1}assignment as well as the peak around 1040 cm^{-1}(Si−O−Si asymmetric stretching modes) were also visualised. For comparison, the researchers also collected FTIR transmission spectra at a spectral resolution of 4cm^{-1}, for a PMMA coating (thickness 5 μm), which depicted the same bands as the s-SNOM setup. However, s-SNOM represents a significant advantage over FTIR in terms of spatial resolution, which is pertinent for nanoscale applications of polymers.

2.1.2 Plasma polymerization coating studies

Plasma polymerization utilizes a plasma discharge leading to the production of excited species which alter the surface energy of the treated surface, creating new binding sites, providing more uniform distribution of functional groups as well as uniform thickness as compared to other coating methods. It is thus suited for making higher precision coatings while minimising solvent use, making it an environmentally efficient process. Plasma polymerization has the added advantage of enabling control of surface properties, such as hydrophobicity and surface energy. For example, Popelka et al [19] investigated the use of plasma polymerization to increase the surface energy of Low Density Polyethylene (LDPE), consequently leading to an increase in hydrophilicity . The researchers added two types of polymers on top of the plasma polymerized LDPE by low pressure plasma treatment: Poly (2-ethyl-2-oxazoline) (PETOX) and PETOX linked to acrylamide groups. These polymers have an important role in increasing the biocompatibility of LDPE by increasing material hydrophilicity, since PETOX contains polar amide, carbonyl and hydroxyl groups. In order to investigate chemical changes induced by the plasma treatments, ATR-FTIR point spectroscopic analysis in the 1800-800 cm^{-1}range and XPS was applied to four samples: untreated LDPE, plasma treated LDPE, plasma treated LDPE coated with PETOX, plasma treated LDPE coated with PETOX linked to an acrylamide group. The plasma treatments generally increased the surface roughness and reduced the hydrophobicity of the LDPE samples investigated. An example where ATR-FTIR may be useful is when the presence of fluorine atoms in plasma polymerized coatings complicates interpretation of XPS spectra of phosphorus related compounds, as it may shift the binding energy of phosphonate groups to the region of phosphate [20]. Furthermore, since ATR-FTIR resolves chemical bonds more clearly than techniques such as XPS, it is particularly useful for polymers, which tend to have more variation in chemical bonding than in elemental composition[21]. The ATR-FTIR

spectra revealed a broad band between 1800 and 1550 cm^{-1} for plasma treated LDPE, indicating the introduction of oxy- and peroxy- groups, while an additional peak at 1630 cm^{-1} was identified for the plasma modified LDPE-PETOX and LDPE-PETOX-acr samples, which was identified as an –N=C=O group. An important limitation of ATR-FTIR here, is that PETOX and PETOX-acr show very similar spectra, because they both contain the same multiple structural unit repeats, calling on the necessity for techniques that can resolve overlapping spectra.

In addition to physical surface modification, plasma polymerization may also give rise to different oxidation states of functional groups on the substrate, in particular for phosphate and phosphonate groups. Siow et al [20] used ATR-FTIR to investigate this diversity in functional groups. Two types of phosphorus containing monomers, triisopropylphosphite (TIP) and diethyl phosphite (DEP) were plasma polymerized directly on ZnSe ATR crystals (coating thickness 10nm). For baseline correction, the reference spectra for TIP and DEP monomers were captured first and then compared to the coated crystals. While comparing spectral features of TIP coated crystal and TIP monomer, several changes in phosphorous related bands were observed, for example, the asymmetric stretch of the P-O-P band at 1000 cm^{-1}(visible in both the monomers and the polymers), P=O stretch at 1220 cm^{-1} due to phosphate or phosphonate(P-O-C bond)(visible in both monomers and the polymers), OH deformation at 1680 cm^{-1} of the O=P-OH bond (appearing post polymerization) and carbon related bands: CH_3 rocking mode at 1140 cm^{-1} of the P-O-CH_2R group(decreases in peak height post polymerization), P-O-C stretching band at 1140 cm^{-1} of the P-O-CH_2R group(visible in both monomers and polymers), symmetric CH_3 deformation at 1370 cm^{-1}(decreases in peak height post polymerization) and the, asymmetric CH_3 deformation at 1380 cm^{-1}(decreases in peak height post polymerization). Similarly, comparison of spectral features of DEP monomer and DEP coated sample showed

significant changes in the following phosphorus related bands: asymmetric stretch mode of P-O-P at 1013 cm^{-1}, (which could also be PO_3^{-2},) OH deformation mode of O=P-OH group at 1680 cm^{-1}(appears post polymerization) and carbon related bands(all carbon bands showed a decrease in peak height post polymerization) : C-C stretch at 961 cm^{-1}, C-O stretch at 1039 cm^{-1} also assignable to asymmetrical P-O-C stretch mode of the P-O-C_2H_5 group, 787 cm^{-1} of symmetrical P-O-C bond indicating oxidation induced by the polymerization process. The authors also compared the results of the ATR-FTIR analysis to a parallel run XPS analysis, where the authors found only phosphate and polyphosphate groups on the surface. The concentration of elements on the surface of the plasma polymerized polymer was estimated using a curve fitting method applied to the XPS spectra. A spatial study to characterize the distribution of phosphate, polyphosphate and phosphonate groups over the substrate would be interesting because, phosphate groups are more susceptible to enzymatic hydrolysis as compared to phosphonates which is a factor in bone tissue regeneration using phosphorous coated scaffolds[22] , therefore, chemical imaging methods that can quantify functional group diversity spatially would be useful.One must also keep in mind that, an ATR-FTIR analysis of plasma polymerized substrates, gives information of the bulk of the sample (micron range), whereas changes brought on by plasma polymerization affects the top few nanometres of the surface of the substrate (10-100nm), so changes brought on by plasma treatment, may or may not be reflected in ATR spectra.

Morent et al[23] used ATR-FTIR spectroscopy (in the 4000-750 cm^{-1}range) to characterize plasma-induced chemical changes on the surface of polypropylene (PP) films (film thickness 75um). Water contact angle and XPS measurements of the PP films were also taken. Plasma polymerization was carried out using a dielectric barrier discharge system in air, which improves

surface wetting and adhesion properties. XPS analysis showed that the air plasma probably broke the C–H and/or C–C bonds, creating free radicals, which react with the activated oxygen species in the discharge leading to the formation of C=O, C–O and O–C=O groups indicating oxidation induced by the polymerization process. Comparing the ATR-FTIR spectra of the plasma treated polymer and untreated polymers, a broad peak at 1738 cm^{-1} appeared in the plasma treated samples, due to the presence of carbonyl C=O groups. A peak at 1647 cm^{-1} also appeared after treatment, which, the researchers speculate, is due to the formation of hydrogen bonds between hydrogen atoms of aldehydes, carboxylic acids and alcohols at the surface, similar to the results produced by the XPS spectra.

None of the studies discussed above, give any information regarding the coating or layer thickness, which is a very relevant parameter for the analysis of the polymer and its subsequent application. For example, it is critical to determine the thickness of the polyethylene glycol like coatings as this can impact coating longevity as a medical bearing surface. However, the potential of vibrational spectroscopic information for thickness estimation has been investigated. For example, an attempt to determine the thickness of tetraglyme (a plasma polymerized analog of polyethylene glycol) on ultra-high molecular weight polyethylene as substrate, was made by Kane et al [21]. Tetraglyme coatings of different thicknesses, 64nm, 108nm, 195nm were fabricated on UHMWPE (Ultra High Molecular Weight Polyethylene) using plasma polymerization. The absolute coating thicknesses found by AFM were then correlated to the area of the most distinct ether peak (at 1115 cm^{-1}) obtained from ATR-FTIR spectroscopy, in order to calibrate the infrared signal so that ATR-FTIR alone could be used to rapidly and non-

destructively calculate the coating thickness of subsequent samples. ATR-FTIR spectra were obtained in the 1800-900 cm^{-1}range using a Ge crystal. XPS and ATR-FTIR spectra were used to confirm the presence of the coating, both of which showed an increase of C=O peak at 1730 cm^{-1}, C-O (ether peak) at 1115 cm^{-1} in the presence of coating. From the calibration curve constructed using AFM data as a reference, the area under the ether peak was directly proportional to the coating thickness, thus giving a predictive thickness measurement, which was validated for coatings polymerized on two different days(R^2 value = 0.97). The thickness estimated through ATR-FTIR differed from the AFM derived thickness measurement by 10-15%. However, this method relies on a number of assumptions such as similarity of chemical composition and density of coatings between samples, constant light penetration depth (which can vary with the crystal pressure on samples) and knowledge of wear behaviour of coating and substrate during scratching. The authors also noted that differences in polymer density or degree of crosslinking of the PEG-like coatings due to variation in the plasma deposition process affects coating thickness by up to 15%. In spite of these limitations, the usage of ATR-FTIR measurements to estimate thickness provides speed & efficiency as compared to repeated AFM measurements for samples which may take longer to perform due to sample preparation and tip preparation/optimization steps. This method can be extended to investigating thickness homogeneity over a wider field of view by spatial imaging. Typically, AFM in tip contact mode is used for polymer or coating thickness measurements in case of polymer on polymer systems. It is challenging to scratch away the coatings without scratching the polymer substrate, implying a difficulty to produce sharp, representative edges which tends to overestimate the coating thickness. In addition, many polymer-on-polymer systems are intended for biological

applications in which they will be hydrated, and a thickness measured in vacuum(as measured in SEM or XPS) is of limited value[21].

2.1.3 Coating Degradation

Polymer degradation is a complex area of analysis, because a cascade of changes can happen over time depending on the immediate environment. Polymers are commonly used as encapsulating materials for systems that perform long term functions (e.g. Solar cells) or shorter term functions (e.g. pharmaceutical) , consequently, the lifespan of the polymer and the nature of its degradation are important in determining its overall functionality. One example is that of a photovoltaic module encapsulated in multiple polymer layers each performing different functions, e.g. protection from environmental conditions, mechanical strength or sealing agents. In one study by Planes et al, the effect of accelerated ageing on the polymeric encapsulation system of a commercially available solar cell was studied by ATR-FTIR mapping and Raman microscopy[24]. In order to identify the different polymeric layers, the infrared and Raman spectra were subjected to PCA. After exposure to ageing (80^{o}C, 85% relative humidity, 0-2000hrs), each of the layers were peeled off, for analysis, by ATR-FTIR mapping and Raman mapping. For the degradation study, only a few bands characteristic to each layer were examined ATR-FTIR analysis revealed de-fluoridation & oxidation on the outer layer & oxidation of the adhesive layers (based on the adhesive layer intensity (C=O bond 1738 cm^{-1}, C-O 1095 cm^{-1} , C-O-C (1017 cm^{-1})The mechanically protective PET layers showed exhibited a in the CH bond (2917 cm^{-1} and 2848 cm^{-1}), and an increase in C=O (1720 cm^{-1}), C-O-C bond (1100 cm^{-1}) indicative of hydrolysis. While the Raman microscopic analysis of the layers, didn't provide information on the bonds mentioned earlier (except the CF bond, which is more polar as

compared to C-O or C=O bond), it did indicate the presence of carbon fillers (2500 cm^{-1}) in each layer (confirmed by a parallel DSC study), which was absent in the ATR-FTIR study. From this one can infer that, typically one technique alone (either ATR-FTIR or Raman Imaging) is not sufficient for analysis of commercial polymeric systems.

A related study byVoronko et al [25]compared one dimensional Raman, confocal Raman and ATR-FTIR to study the uniformity and thickness changes of an adhesive layer in the cross sections of a multilayer laminate under different weathering and ageing conditions. Significant changes in the position and functional groups of the adhesive layer were tracked by all three methods. Raman line scans were faster in comparison to Raman Imaging, but Raman Imaging, provided a quantitative estimation of the change in adhesive thickness. The results provided by Raman Imaging were more accurate than ATR-FTIR, due to the higher spatial resolution (1um) obtained as compared to the spatial resolution of the ATR-FTIR system (9um). Moreover, Raman imaging resolved the ester group of the adhesive (632 cm^{-1}) better than ATR-FTIR. As the authors mention, chemical imaging enables improved analysis of spatial variations in the imaged surface and chemical properties associated at a particular point on the image (imaging allows identification of regions containing specific targets (e.g. adhesive), while the spectroscopic dimension provide functional analysis of the target). This research is supportive of imaging using Raman line scanning for tracking changes in a single adhesive line in a less time consuming manner as compared to wide field Raman Imaging, however, Raman Imaging is potentially more useful as the extent of the adhesive component cannot be resolved optically and spreading of adhesive cannot be visualised using line scans.

Most of the studies mentioned earlier involve surface studies of polymeric systems. Depth profiling of the degradation of a coating is also important, for example when polymers are applied in paints, the coatings get exposed to many environmental conditions. Zhang et al used confocal Raman microscopy[26]to characterize melamine based coatings (20um) on a titania substrate at different depths and weathering conditions The coating was subjected to UV weathering treatments (340nm 3000h at 50 deg C/100% RH) and measurements were taken at 5 different time periods (500h, 1000h, 2000h, 2500h, 3000h). From the comparison of the control coating (unweathered) and weathered coating, a reference band at 950 cm^{-1}(which stayed constant, regardless of treatment), and a melamine representative band (980 cm^{-1}) were selected. In order to model melamine degradation at different depths and weathering exposure times, the normalised melamine ratio, i.e., area under the peak for the melamine band (980 cm^{-1}) to the area under the peak of reference band (950 cm^{-1}) was selected**.** The authors noted three shortcomings in the use of Raman microscopy for this application: it works only for clear coatings (titania appears opaque), depth profiling is limited to depths of 0-25um range and is time consuming (2 seconds per pixel) if a step size of 1um is chosen to model the degradation. Despite these shortcomings, changes in the normalised melamine ratio, indicated that coating degradation mainly occurred until 10um depth, and deeper layers remained unaffected. The authors also noted that the decrease in degradation could also be linked to the decreased diffusion of moisture and decreased availability of oxygen for free radicals (generated by the UV weathering) to damage deeper layers. The increase in oxygen and moisture related bands as degradation proceeded (beyond 2000h) to deeper depths, was found by an SSPA/FTIR (step-scan photoacoustic/FTIR) study, run parallel to the same experiment. In a typical SSPA/FTIR experiment, a sample kept in a closed chamber surrounded by a carrier gas, is irradiated by a

laser, the heat generated on the sample warms the carrier gas, which in turn is interpreted as an acoustic pressure wave by a transducer[27]. SSPA/FTIR was chosen, because, of the correlation between photoacoustic frequency and sampling depth, allowing non-destructive yet controlled depth profiling(depth resolution 2um) and ability to detect carbon and oxygen related bands(which Raman imaging cant study to the same extent as referenced by[24]). The authors note that, SSPA-FTIR provides more information in terms of functional group changes, as degradation proceeds, yet, the resolution at which these are studied, and therefore, the reliability of the results, are less accurate as compared to confocal Raman microscopy (which has a higher depth resolution of 1um).

In the field of biomaterials, Jing et al [3] investigated the use of ATR-FTIR imaging coupled with PCA to study the degradation of a biocompatible blend of poly L-Lactic acid/Hydroxyapatite created by solvent casting. PLLA/HA composite materials were immersed in phosphate- buffered saline (PBS) solution (pH 7.4), a biomimetic solution, at 37°C for in vitro degradation over a period of 105 days and scans were taken every 7th day. Initially a univariate approach was taken to visualise the distribution of PLLA as shown in Figure 6.

----------FIGURE 6 GOES HERE----------

The degradation process was modelled using 1025/1755 cm^{-1}ratio of the PO bond stretch (hydroxyapatite) to the C=O stretch (PLLA). Portions of the sample were cut, rinsed using deionised water, dried and imaged using a Si ATR crystal. Different spatial areas on the sample were imaged to capture more representative degradation. PCA was applied on the spectral data,

resulting in 8 PCs, where the PC1 captured 90% of the variance. The 1025/1755 ratio was selected because these bands showed the most changes when PC1, PC3, PC4 were plotted against the degradation time (0 to 105 days) The PC2 loading plot against degradation time, exhibited water peaks in IR spectrum indicating adsorption of water by the material. This study demonstrates how loading plots of the PCs could be employed in selection of the wavelengths affected most by the degradation process. However, no reference method such as DSC or TGA was utilised to compare the results obtained for the degradation process.

2.2 PHASE DISTRIBUTION in multi-material polymer blends

In the case of multi-material polymer blends, obtaining insight into phase separation behaviour, non-destructive characterization of local morphology and chemical composition are all important. Constituents in the blend can be organised in continuous, semi- continuous or dispersed arrangements, which can manifest different structural or chemical behaviour.. It is also of interest to understand how this organisation can change with respect to the conditions the blend is exposed to. Using chemical imaging it is possible to study patterns of change in the polymer blends due to heat, moisture, radiation or chemical attack. Some representative examples are provided below.

2.2.1 Graphene and Single Walled Carbon Nanotubes (SWCNT) embedded in polymers

In a recent study by Shojaee et al[28], the dispersion of graphene platelet aggregates (GPLs) with sizes ranging from 1 to 4.5 um (as a function of different concentrations of GPLs) in a “Bisphenol A” blend epoxy resin was investigated using confocal Raman imaging. These GPLs when mixed with polymers provide enhanced mechanical strength at very low concentrations,

but suffer from the problem of graphene sheet entanglement. The agglomeration of the GPLs decreases the interfacial contact area of the graphene filler and reduces its effectiveness in enhancing the mechanical properties of the polymers. Therefore it is important to study the dispersion of the GPLs in a polymer blend. In the study, different GPLs concentrations (0.05%, 0.1%, 0.2%, 0.3%, and 0.4%) were mixed with the epoxy resin and three different Raman signatures, the G band at 1500–1700 cm^{-1}, the D band at 1250–1450 $cm^{-1}$and the first overtone or the 2D band at 2600–2800 cm^{-1} (all three are carbon based bands but relate to different agglomerate sizes) were used to identify the GPLs. The Raman spectra were obtained at room temperature in reflection mode using a frequency doubled Nd:YAG laser (532nm), which offered a high spatial resolution of 0.36um, (which is more than any of the earlier systems discussed here) over an imaging area of 30 x $30um^2$. The average agglomerate size was obtained by dividing the total area exhibiting graphene Raman modes on the image by the number of agglomerates in the image. Then, assuming a circular geometry for the agglomerates, the average size was calculated. The results showed a constant increase in the average agglomerate size of graphene with increasing graphene concentration leading to a higher volume of weak regions in the specimens. This study demonstrates the major advantage of confocal Raman microscopy as compared to standard methods such as Transmission Optical Microscopy in that it can be used to identify the graphene signature and its spatial distribution within a composite structure, non-destructively and without significant sample preparation.

In a related study[4],the morphology of SWCNTs (Single walled carbon nanotubes, length = 100 – 1000nm, diameter = 1nm) dispersed in a B-Staged epoxy resin thin film (50um thickness) was analysed by Warren et al using confocal Raman imaging (632.8nm laser excitation wavelength). Oxidation and functionalization of SWCNTs are two approaches used to increase the dispersion

of pristine SWCNTs in a polymer blend. The dispersion and alignment of the SWCNTs determines the mechanical and tensile strength of the blend, to be used as packaging for microelectronics or as coatings. The thin films were incorporated by three chemically distinct SWCNT species at a loading concentration of 0.5% by weight for each: oxidised SWCNTs (oxidised by a mix of sulphuric acid and nitric acid), functionalised SWCNTs (functionalised with a dendrimer), and pristine SWCNTs (in their native state). Thin films prepared from these three types of SWCNTs were compared to each other as well as a pure epoxy sample, to look for dispersion and alignment. The G-band characteristic of CNTs at 1580-1590 $cm^{-1}$was utilised for identification of SWCNTs. DSC was used to understand the curing process of the resin and tensile testing was undertaken to characterize the thermo-mechanical behaviour of the resinresults to compare with Raman imaging. The dispersion analysis of the SWCNTs using Raman imaging was compared with scanning electron microscopy (SEM) and transmission electron microscopy (TEM), and while the both scanning and electron microscopy required sample preparation, and were destructive, Raman imaging required no sampling, was capable of imaging the whole surface, was relatively less destructive, but limited in terms of its spatial resolution, which is a function of the size of the focused laser beam. To circumvent the problem of lower spatial resolution compared to other microscopy techniques, the authors recommend imaging samples at smaller sampling steps than the laser spot size, which facilitates a higher resolution as compared to the native resolution. The authors used two ways to visualise the SWCNT dispersion, first, by plotting the G-band distribution over the scanned area, and secondly, using the reference Raman spectra of SWCNTs and epoxy matrix to deconvolute the hypercube into two components and present their distribution in a single chemicalimage(**Fig 7**).

----------FIG 7 goes here G band distribution Warren et al----------

After analysing the outputs of the two methods, they determined that the first approach allowed better visualisation of high nanotube concentration regions, whereas the latter was better for regions with small amounts of nanotubes. Visualising the dispersion of nanotubes in epoxy based blends using Raman imaging was shown to be useful because, the nanotubes give sharp peaks (G-bands) whereas, the epoxy matrix in the samples give structure-less Raman responses(mostly fluorescence). However, conventional techniques such as SEM and TEM offer a higher degree of information regarding the morphology of a polymeric blend being analysed (such as pore size of polymer used, absolute values of SWCNT dimensions), which conventional Raman Imaging cannot yet deliver.

2.2.2 Crystallinity

Crystallinity, phase distribution and dispersion are important properties of polymeric blends. Phase changes due to polymer post processing steps are of interest to the industry and tools that can non-destructively monitor these phase changes are required. In this section we review recent studies where chemical imaging was used to investigate crystallinity and phase dispersion.

Izumi et al[29] examined a biodegradable polymer blend of Poly-R-3-hydroxy butyrate (PHB) & poly[(R)-3-hydroxybutyrate-co-(R)-3-hydroxyvalerate (PHBV). PHBV was added to improve the mechanical strength and melt processing ability of PHB. Fourier Transform-Raman spectroscopy was used to study the change in crystallinity of the copolymer blend in response to controlled changes in temperature (from 25 to 175 ^{o}C). Blends with different concentrations (5%, 8%, and 12% of hydroxyvalerate in PHB) were compared against the homopolymers. Spectra from different spatial locations of diameter 200um^{2}, were scanned and averaged. The full width at half height of the band centered at 1725 cm^{-1}(C=O bond in the crystalline state of PHB,

PHBV) was used toestimate the degree of crystallinity in film samples. Conventionally, DSC is considered to be the standard method to analyse the crystallinity of polymers (inferred from melt characteristics), while NMR is suitable for studying the size of crystalline domains of polymers as well as their concentrations. In this study, DSC data was used to measure the crystallinity degree ($W_{c,h} = \frac{\Delta H_m}{\Delta H_{m\,0}}$, where $W_{c,h}$is the degree of crystallinity, H_m represents the heat of melting of sample and H_{m0} represents an absolute value of $146 Jg^{-1}$, the heat of melting of 100% crystalline polymer) while NMR was used to evaluate composition of the blends. These methods were used in conjunction with the FT-Raman study of the blends. Changes during melting process of PHB and PHBV were monitored by recording FT-Raman spectra of PHB and PHBV at different temperatures. The authors reported that it was not possible to correlate the intensity changes of these bands (1443 cm^{-1} CH_2 bend, 1458 $cm^{-1}CH_3$ asymmetric bend) with the composition of the films, because the films presented different crystallinity at different spatial locations that exerts influence in the Raman intensity of these bands.In this case, a spatially resolved study using Raman Imaging could be useful to investigate spatial variation in crystallinity, which is not possible with DSC.

In a study by Kljun et al[30], ATR-FTIRwas used to study change in crystallinity of cotton fibres, from cellulose I to cellulose II in response to alkaline conditions. This conversion from a less stable parallel chain form(cellulose I) to a more stable non-parallel chain form(cellulose II) is an important process in the textile industry referred to as mericerization. ATR-FTIR spectra were collected for cotton samples exposed to NaOH solutions for defined time intervals. The change in crystallinity was observed by an index of crystallinity by monitoring the change at

1430 cm^{-1}(cellulose 1) and 893 cm^{-1}(cellulose 2). This method was also compared to XRD (X-Ray Diffraction) and imaging based on cellulose binding fluorescent probes. For the fluorescent probes method, sample preparation was cumbersome, as ethanol, acetone and ether treatment to remove wax content of the cotton fibres for over 5 hours was required. However, regardless of the time consuming preparation method required, the authors demonstrated that the cellulose binding probes offered greater sensitivity(level of crystallinity = 0.7) as compared ATR-FTIR or XRD because of its sensitivity to low concentrations of alkali. Considering ATR-FTIR and XRD, ATR-FTIR was less sensitive to the effect of alkali treatment on crystallinity (lowest index of crystallinity detectable = 1) compared to XRD (lowest index of crystallinity detectable =0.8) for the same cotton sample. A disadvantage of XRD ,is that while studying the crystallinity change of cellulose fibres, the XRD process changesthe crystallinity of the fibres during sample preparation, which affects textile processing whereas ATR-FTIR does not[30].

NIR imaging (900-1700nm, 30um spatial resolution) in conjunction with multivariate analysis was carried out to analyse the spatial distribution of polymer crystallinity in HDPE(High Density Polyethylene), LDPE(Low Density Polyethylene) and PP(poly propylene) by Gosselin et al[5]. Sample size for the polymeric films created from compression moulding were 100mm x 40mm x 1.5mm. Samples were subjected to a range of 30 – 200 °C (heating rate of 10 °C/min) and with different cooling rates (1- 16°C/minute) to create a set of samples with different degrees of crystallinity. Different chemometric strategies were used to analyse the polymeric blends, employing spatially averaged spectra, derivative pre-treatments, multi-way principal component analysis and image regression to predict distribution of crystallinity. From a comparison of the different chemometric strategies, the authors deduced that overall multi-way principal component analysis was optimal in terms of prediction power(**Fig 8**).

----------Figure 8 goes here----------

This paper demonstrates how the combination of multivariate analysis and NIR imaging can be used to estimate the spatial distribution of crystallinity over a sample as compared to point scanning techniques.

Using NIR imaging in transmittance mode(6.25um spatial resolution, 4900-4600 cm^{-1} range), Shinzawa et al[31], quantified the change in crystallinity in PLA films with different percentages of organically modified clay (0-15%). The change in crystallinity was verified by thermomechanical analysis (TMA) and DSC. Although the clay used (montmorillonite) doesn't exhibit any distinct peaks in the NIR range, changes in peaks at 4770 cm^{-1}, probably arising due to the combination mode associated with terminal OH groups of PLA (which is perturbed by the addition of clay), could be used to monitor changes in crystallinity. The authors stated that band shift mapping for specific bands is more reliable as opposed to a multivariate analysis(such as PCA) to bypass any capture of noise in the latent structures arising from the application of an algorithm like, PCA on the hypercube. Through the use of third derivatives of the spectra, very small band shifts were observable. It was observed that the inclusion of clay substantially increased the frequency of the spontaneous nucleation of the PLA crystals and a corresponding decrease of the amorphous portion resulted in less elongation of the samples (measured by TMA) during the heating process under a certain level of load. Again, the authors state that, using an NIR imaging technique, spatial variation of polymeric samples is more representative of the samples being analysed as compared to point spectroscopic methods. The authors applied PLS regression models to the data using different spectral pre-treatments.

More recently, Ishikawa et al[6], NIR reflectance imaging was utilised for the prediction of crystallinity and concentration of PLA in PLA/PHB blends, and the results agreed with XRD measurements. The authors clearly highlight the advantages of NIR imaging in polymer analysis over XRD and point spectroscopic methods i.e. non-destructive and non-contact evaluation and observation of spatial variation of polymer indices such as degree of crystallinity. The polymers used, PLA and PHB are environmentally friendly and produced from renewable sources, therefore their characterization is highly relevant for their use as biocompatible materials. PLA/PHB blends of different ratios (100/0, 80/20, 60/40, 40/60, 20/80, 0/100) were studied. In addition, six films of pure PLA of differing annealing conditions were also created as a reference for crystallinity measurements using XRD. To understand crystal evolution and crystallinity, the films were exposed to a temperature range of 70-105°C, and to avoid moisture absorption by the sample during measurements, wooden blocks were placed around the sample stage, during NIR imaging acquisition. Various overtone and combination bands in the 1600-2200nm range were analysed and PLS models were developed to predict crystallinity and concentration of PLA in the blend using three different methods: absorbance data, second derivative spectra, and SNV spectra. The SNV pre-treated spectra produced the best prediction of crystallinity($R^2 = 0.98$) since it standardises the effect of different intensity influenced by thickness and homogeneity of samples**(Fig 9)**.

----------Fig 9 goes here----------

It is important to note here that, the custom built NIR imaging unit used by the authors gave a high field of view (150 x 250mm^2) and low scan time of 5 seconds, which is a significant

advantage over XRD, a method that can take many hours per analysis depending on scan parameters. A limiting factor with this system was the low spatial resolution of 0.25mm/pixel.

A newer imaging technique called TERM (Tip Enhanced Raman Mapping) was employed [32] to analyse the phase distribution on a PMMA(poly(methyl methacrylate))/SAN(poly(styrene-co-acrylonitrile)) based copolymer blend. TERM offers a very high spatial resolution of 20-30nm, which enables distinction of nanoscale features. Blends were annealed at 250^{o}C for 2min (film 1) and 5 min (film 2), respectively, to induce phase separation, followed by quenching at room temperature. The induced phased separation was monitored using confocal Ramanimaging , Tip Enhanced Raman Spectroscopy (TERS), and Tip Enhanced Raman Mapping (TERM). AFM was used for morphology comparisons, but samples required chemical etching before they could be analysed. Two bands, specific to PMMA (C-C stretch at 800 cm^{-1}) and SAN (phenyl ring stretch 1002 cm^{-1}) were used for analysis over a spot size of 10um x 10um. The same laser excitation wavelength (633nm) and exposure time (5s/point) was used to analyse the film surfaces. Changes in interphase location, phase inversion and interphase distances were visualised by TERM which offered 1500 times the enhancement factor(pixel size 8nm, 1umx1um scan area) as compared to conventional Raman imaging, using a smaller spot size (1um x 1um). Even though, as the authors mention, a low power laser setting was used in the TERM measurements, since the imaging area is reduced, local heating effects became more pronounced, affecting the phase separation of the blend. This is a potential shortcoming of TERM measurements, higher spatial resolution is available but at the cost of modifyingthe sample. The authors also state that, for measurements taken over the course of a few days, a constant TERM enhancement factor is required, which is difficult to attain due to a limited field enhancement by localised

plasmons[33]**.** Moreover, reproducibility and availability of gold tips required for TERM measurements is still an issue. [34]

2.3 Compositional studies

In a study by Brun et al[35] applied Raman imaging (785nm NIR laser) was used for quantification of polybutadiene in polystyrene pellets. The addition of polybutadiene in polystyrene can increase the fracture resistance of the polymer, and the microstructure of polybutadiene (cis or trans form) can affect the degree of branching in a polymer. In this study, different approaches were used to predict the concentration of polybutadiene (rubber) in polystyrene as measured by proton NMR based analysis of the sample. The polymeric blends created contained different concentrations of polybutadiene (ranging from 0 to 10% by weight) and had general dimensions of 2mm x 2mm. The authors employed two methods to quantify polybutadiene in the polystyrene pellets: a curve fitting method, which uses a few characteristic bands (1000 cm^{-1}, 1157 cm^{-1}, 1492 cm^{-1}) to visualise dispersion and a PLS based chemometric method. The authors mention that the curve fitting procedure suffers from the obvious disadvantage, that one needs to hunt for a very specific butadiene Raman signature for analysis, and this process is a time consuming, iterative process. Furthermore, Raman spectroscopy is very sensitive to the carbon double bond stretching of 1, 2-vinyl, 1, 4-cis, and 1, 4-trans polybutadiene (1644 cm^{-1}, 1656 $cm^{-1}$and 1671 cm^{-1}, respectively), as is C13 NMR analysis (instead proton NMR was carried out by the authors in the study, which has even lower sensitivity to the mentioned bands), but Raman spectroscopy has a lesser sampling time.The authors finally conclude that, although both prediction methods (curve fitting and chemometric analysis) gave

similar results in terms of prediction of polybutadiene in polystyrene, chemometric analysis coupled with Raman imaging, was more efficient (calculations within seconds, lower bias, higher reproducibility) and practical for the study of polymeric blends.

Using *Broadband CARS imaging Lee et al*[7] investigated the location of a compatibilizer in polymer blend. The compatibilizer styrene-ethylene/propylene (SEP) copolymer was utilised to make the polystyrene (PS), polypropylene (PP) multilayer polymer blends more miscible with each other. The blend thickness varied from 50um to 75um. Peaks at frequencies of 1000 cm^{-1}, 2880 cm^{-1} , and 2850 cm^{-1} for PS, PP, and SEP were used to qualitatively visualise the components of the blend (**Fig 10**), even though some spectral overlap in the Raman signature was noticed, particularly for SEP, which shares styrene and propylene units(monomers of the polymers used).

----------Figure 10 goes here----------

In order to quantitatively analyse the concentration of each component in the tertiary blend in the presence of spectral overlap a four step processing method, comprising of singular value decomposition (SVD), modified Kramers-Kronig (KK) phase retrieval, baseline de-trending, and classical least squares (CLS) was proposed. The authors state that, the analysis of broadband CARS spectra, though challenging, provides significant advantages over SEM. Cryofacture and microtome derived thin slices are required for SEM analysis, which suffer from inability to localise cryofracture at certain spots specifically and loss of image contrast respectively, both of which ultimately alter the native state of the blend. Moreover, B-CARS, is a nonlinear technique, which benefits from a higher Raman signal (compared to conventional Raman imaging) leading to high signal to noise ratio and uses multiple frequency beams, allowing better quantitative

analysis compared to single frequency methods (CARS microscopy only or stimulated Raman scattering microscopy only). A limitation of the CARS technique, as noted by the authors is that, the CARS and non-resonant background signal cannot be measured at same position on the sample, althoughthis fact is disputed according to Lee et al[7]

Time resolved CARS or tr-CARS was recently used as an alternative to chemometrics in resolving overlapping peaksin a pioneering study by Kotiaho et al[8], to study micro particle dispersion in a thin film polymeric blend. The hypercube formed in this case had four dimensions: x,y = spatial, z= spectral and t= time domain. Representative figures from the study illustrating the distribution of microparticles and the propylene matrix at different probe delays are shown in Figure 11.

----------FIGURE 11 GOES HERE----------

The characterization was qualitative in nature but confirmed the possibility of imaging chemicals which otherwise compared to give rise to the same signal in a Raman based study. This was evidenced by the distinction of octamethyl polyhedral oligomericsilsesquioxane (referred to as om-possmicroparticles) and polypropylene, both of which give a signal overlap at C-H bond. The CH stretching region is often congested with multiple overlapping bands when organic compounds are measured. Since CARS is a non-linear imaging technique, coupling it with time domain measurements allowed the researchers to find a unique temporal signature for every chemical entity in the blend. Time resolved Raman Imaging techniques, also offer another advantage ; they can resolve samples with high fluorescence[36]. The authors concluded that tr-CARS had a huge advantage over linear imaging methods for cellular systems, and interactions of the cellular systems with chemicals. However, improvement in terms of optimization of

spectral widths of pulses and other instrumentation parameters need to be improved, to increase signal to noise ratio.

In another study by Bonifacio et al[17], confocal Raman microscopy (632.8nm laser excitation) was utilised to semi-quantitatively map biochemical constituents such as collagen, non-collagen protein, proteoglycans, nucleic acid in articular cartilage tissue of 100um thickness. This study is important in tissue engineering applications, because it investigates the use of chemical imaging techniques to study the extracellular matrix, whose destruction signals the beginning of degradation in many disease models. The authors noted that Raman imaging is more suitable for studying ECM components as compared to FTIR, [37]because below 2000 cm^{-1}, water shows a weak signal, allowing study of native tissues. The authors used a chemometric approach and compared four classification techniques: PCA, PLSR, hierarchical cluster analysis (HCA) and fuzzy c-means cluster analysis (FCA). After PCA analysis of the hypercube, two principal components were selected which explained most of the spectral component variance. In order to cope with the daily drift of the spectrograph, requiring recalibration of the grating position, resulting in different Raman shifts for the measured data points of the model substances versus spectra of the tissue sample, the authors used a 'loess' smoothing procedure on the Raman spectra (for PLSR calibration), which also improved the signal to noise ratio. The authors mention that collagen orientation (parallel and anti-parallel) can affect spectra, and this is noticed in both FTIR imaging in a different study as well as Raman imaging[37]. Standard deviations of the Raman maps were used to deduce information regarding different collagen constituents (modelled using alpha helix band at 1656 cm^{-1}, and beta sheet band at 1670 cm^{-1}, secondary

structures of collagen, an important constituent of the ECM), calcium carbonate deposit band at 1087 cm^{-1}, and non-collagen constituents (bands of aromatic amino acids, tryptophan, tyrosine and phenylalanine).Further , by mapping the sum of intensities at Raman shifts which are characteristic of each different biochemical constituent, the authors were able to show that the intensity sum calculated over intensities at 1578, 1488 and 782 cm^{-1} for DNA, at 1380, 1342 and 1068 cm^{-1} for chondroitin sulphate, at 1271, 1246, 920, 857 and 816 cm^{-1} for collagen and at 1555, 1127 and 1004 cm^{-1} for non-collagenous proteins over Raman images. The authors demonstrated that while PCA was excellent for differentiating cells, ECM and collagen at a low computational cost, the PLSR model could differentiate effectively between different protein secondary structures. FCA turned out to be better than HCA at recognising collagen/proteoglycan ratio in the ECM, and HCA suffers from the inability to monitor in-class differences in spectra. The authors noted that Raman mapping is complementary to FT-IR imaging, and it is particularly suited in studies where spatial resolution is important, and single cells are to be resolved, at the cost of higher collection time. In this study it is shown that, Raman chemical images are better than bright field microscopy to identify cells whenno morphological feature is present, and easy recognition of DNA bands in nuclei is possible.

2.3.1 Characterization of pharmaceutical polymers

Drug loading on polymeric substrates is a domain well suited to NIR-chemical imaging and Raman Imaging due to minimal sample preparation and quick analysis. In the following section, some representative examples of infrared and Raman imaging coupled with chemometricsto provide spatial information on the drug loading and distribution are given.

The spatial distribution of drugs on polymeric systems using chemical imaging is a well investigated area. An example is theophylline, a natural anti-asthma substance found in cocoa beans and used to treat respiratory problems. Hydrogels containing theophylline constitute a new class of biocompatible drug delivery systems**.** Oprea et al [9] investigated the use of NIR chemical imaging (transmission converted to absorbance, 1000-2500nm range) to study the loading degree of theophylline in a Xanthum/Chondroitin sulphate(X/CS) hydrogel mix. Three hypercubes were captured: pure theophylline, X/CS (50:50 ratio) hydrogel, X/CS (50:50 ratio) hydrogel loaded with theophylline and were compared to analyse theophylline distribution and loading. In the NIR CI study, a number of overlapping peaks were encountered for the hydrogel and the theophylline, the authors therefore, suggested the use of chemometric analysis to resolve drug distribution in samples. PCA and PLS-DA were used to determine principal components, and predict drug loading respectively. A slight shift of bands position from 1717 to 1720 $cm^{-1}$and from 1667 to 1670 cm^{-1} attributed to -CO-N(R)-CO- theophylline characteristic group was used to confirm drug loading and could be visualised from chemical maps (**Fig 12**).

----------Figure 12 goes here----------

Similarly, FT-NIR transmission imaging was utilised to study the quantification of constituents on thin films produced by solvent evaporation comprising of HPMC(hydroxyl propyl methyl cellulose), PVP(poly vinyl pyrrolidone) and PEG loaded with paracetamol [38]. Seventeen formulations were prepared with differing amounts of polymers and paracetamol based on a D-optimal experimental design. Since solvent casting results in films of varying thickness and thus variability in the spectra, the authors suggested the use of the Savitzky-Golay algorithm with first derivative, a common data smoothing technique, to improve accuracy and reduce effects of

scattering. Wavenumber ranges 6083–7800 cm^{-1} and 5276–5364 cm^{-1}were excluded before PLS model development, as these comprised mainly of noise. Predictions at pixel level were carried out by applying the respective PLS model for each constituent in the sample. Concentration maps from PLS models were obtained directly from the spectra of the pixels with an RMSEP of 4%, whereas for quantification by Multivariate Curve Resolution - Alternating Least Squares(MCR-ALS), linear regressions pixel-to-pixel were done previously to construct images, resulting in an RMSEP of 5%. The chemical maps in Figure 13, show the heterogeneity of the different components in the formulations.

----------FIGURE 13 GOES HERE----------

Raman imaging (excitation wavelength: 785nm laser, 3200-600 cm^{-1} range, 4.2mm^2) was used in a study byBreitkreitz et al[39] to evaluate the homogeneity of Atorvastatin Calcium drug in a hydrophilic and lipophilic polymer complex copolymer blend. Rather than using a univariate approach, the multivariate approach of PLS was employed to predict the concentration of each component of the blend. Validation of PLS model and the selection of the number of latent variables (LV) was carried out by a leave-one-out cross-validation procedure. The predicted concentration of an added surfactant (Gelucire) in the pixels varied from 71.7 to 81.3% and 21% to 31.3% for the drug and the polymer component. However, no method of comparison was utilised to support the results;a reference method such as mass spectrometry could be useful to confirm results.

In another study by Nita et al[10], the drug loading of Indomethacin in a pHEMA(Poly(2-hydroxyethyl methacrylate) polymer matrix, including colloidal drug protectors, was evaluated using NIR imaging complemented by TGA/DSC for thermal analysis, dynamic swelling studies

for swelling behaviour and SEM for phase study. The main advantage offered by NIR imaging was its non-destructive nature and lack of sample preparation as opposed to SEM (which involves cryofracture of blend) and TGA. Evaluation of drug loading degree and indomethacin/polymeric system homogeneity was estimated by PLS-DA (Partial least squares - Discriminant Analysis) & MCR. Figure 14, depicts the predominantly homogenous distribution of the drug, Indomethacin in the polymeric matrix containing primarily pHEMA and dispersive colloids such as PVA (poly vinyl alcohol), PAS (poly aspartic acid) and cyclodextrins.

----------FIGURE 14 GOES HERE----------

In all cases of pharmaceutical analysis reviewed, chemometric analysis was useful for development of predictive models. NIR imaging is faster in data acquisition as compared to Raman imaging, which could be more relevant to in-line monitoring of pharmaceutical manufacturing firms. Another difference between the twomodalities, is the difference in spatial resolution offered by each, for Raman imaging systems a resolution of 0.5um, while NIR imaging typically enables a resolution of less than 20um.

2.4 MOISTURE CONTENT

The presence or absence of moisture in polymers can be easily monitored using IR and Raman Imaging. Some examples are discussed in this section.

In a recent study by Small et al [40], the moisture content of polyamide 66 was predicted using Fourier Transfer Near Infrared (FTNIR) spectroscopy in transmission mode. The average sample

dimensions were 25mm x 20mm x 0.4mm and were exposed to 0-100% moisture uptake using randomised methods of moisture exposure (soaking polymer in water, placing in a humidified chamber, exposing sample to ambient laboratory conditions) over a time course of 6 months. Reference mass measurements were taken using an analytical balance to measure increase in moisture. TGA measurements for changes in mass were also compared to analytical balance mass measurements, and were well correlated (percentage difference between the two ranged from -1.65% to +0.78%), therefore authors used mass balance data to construct models. Increase in band intensity at 3300 cm^{-1}(fundamental O-H stretch) and 5200 cm^{-1} (combination band of O-H fundamental stretch and bending) indicate uptake of water. Spectra were normalised using Standard Normal Variate (SNV) and PLS calibration models were developed in the 5000-4000 cm^{-1}range. Upon uptake of water, the overtones and combination peaks of polyamide 66 that arise due to the amide linkage are expected to deviate as a result of hydrogen bonding, which was used as the basis for moisture prediction**.** The calibration model showed good prediction results (SEP values ranging from 0.96 – 1.93%) although the authors note that, a prediction bias appears for longer duration moisture measurements.

The performance of a polymer electrolyte fuel cell (PEFC) depends on proton conductivity and state of hydration around the membrane[41]. They also state that conductivity is related to membrane morphology and acidity of sulphonic acid groups which is also, related to water content. In order to establish a relation between water content and proton conductivity, time resolved point spectroscopic ATR-FTIR (4000-1400 cm^{-1}) to monitor change of water spectra (HOH band 1740 cm^{-1}, 1630 cm^{-1}, ATR-FTIR N_2 purge, Ge crystal n=4) and conductivity measurements (milliohm meter) were carried out on PEFCs[41]. Spectra were collected during hydration/dehydration cycles of 3h exposure to dry N_2, 3h exposure to humid N_2 and 3h

exposure to dry N_2 again. During the hydration state, complete dissociation of SO_{3-} H^+, hydrated by protons, exhibiting a HOH vibration mode at 1740 cm^{-1}, with no change in proton conductivity was noticed, followed by proton conductivity increase with band component at 1630 cm^{-1}, assigned to water associated with SO_{3-} ions during hydration. Conductivity and the 1630 cm^{-1}band decreased very quickly within 10-20min of dehydration. This was quantitatively analysed by plotting conductivity and band area of 1630 cm^{-1}. A linear relationship between conductivity and band area of 1630cm^{-1} was identified.

An interesting aspect of water is the possibility of finding free and bound water molecules, which show different behaviour around membranes. The PEFC Nafion contains 3-4nm water channels, and the presence of free and bound water molecules around these water channels was investigated by the use of AFM-IR[11]. Nafion was cryo-microtomed to a thickness of 300nm and imaging was carried out using AFM-IR over a 3 µm x 3 µm scan area, correlated to a pixel size of 6 nm × 6 nm, over a 3600-2700 cm^{-1} range under ambient conditions (R.H. 50%, 24 °C) with a spectral resolution of 16 cm^{-1}. An OH-stretching peak of free (bulk-like) water, bH_2O, at 3482 cm^{-1} and bound water, iH_2O, adjacent/or near the hydrophilic sulfonic group at 3211 cm^{-1} were visible in the AFM-IR spectra. For comparison, ATR-FTIR measurements taken at a 4 cm^{-1}spectral resolution, only displayed the OH-stretching peak of free (bulk-like) water, bH_2O, at 3482 cm^{-1}.

----------INSERT FIGURE 15 here----------

Furthermore, the AFM-IR spectrum after thermal treatment at 135 °C for 13 h to dehydrate the sample showed that the bound water peak at 3211 cm^{-1} has dropped in intensity, while the intensity of the free water at 3482 cm^{-1} remained unchanged. This behaviour was interpreted as

readsorption of water to the surrounding environment during the cooling process just after the thermal dehydration treatment. The authors mention that, this represents a significant advantage over ATR-FTIR measurements which are less sensitive to surface changes, as ATR-FTIR only detects at least two micrometers of bulk water from below the Nafion surface.

2.5 Protein conformation on polymer surface

Considering studies using synchrotron based imaging, Ling et al[42] utilised FTIR imaging in transmission mode to investigate the conformation of silk fibroin (SF) protein in a SF/PEO (poly ethylene oxide) blend and the phase separation behaviour. Scanning Transmission X Ray Microscopy (STXM) was used as a reference to compare the results from FTIR imaging. FTIR imaging is more sensitive to protein conformation but with lower spatial resolution and greater tolerance to thick sample films, while on the other hand, STXM imaging has higher resolution, more quantifiable composition mapping and better tolerance for thinner sample films. Thin films for FTIR imaging had a thickness of 5um, but STXM required a 100nm film thickness for effective characterization. Gaussian models were used to monitor band shape and band width adjustments of amide I (1700-1600 cm^{-1}) and amide II (1600-1500 cm^{-1}) bands (characteristic of SF) which were further normalised and analysed using k-means clustering. For the phase distribution, a PEO specific band (carbonyl stretch 1000-1184cm^{-1}) and SF specific band (amide II bands 1500-1600 cm^{-1}) were used. In order to account for differences in thickness of the cast films, the ratios of absorbance of SF to the absorbance of PEO were integrated. Three different types of films were analysed: film 1 containing alpha helical conformation of silk fibroin, film 2 containing beta sheet structures of silk fibroin (film 1 treated with 70% ethanol solution) and film 3 containing SF/PEO only. Film 1 gave absorption bands at 1660 cm^{-1} and 1540 cm^{-1},

indicative of random coil/helical conformation, film 2 gave absorption bands at 1630 cm^{-1} and 1540 cm^{-1} indicative of beta sheet structures (1700 cm^{-1} for antiparallel beta sheet), while film 3, gave no such absorption bands, confirming the use of amide bands as markers for silk fibroin. The bands above were used to map the phase distribution effectively, but spatial resolution became difficult for morphologies smaller than 4um, due to the diffraction limit of the FTIR imaging system. Hereon, STXM was used to study smaller morphologies. STXM was more sensitive due to a higher spatial resolution of 30nm compared to FTIR imaging and to changes in water absorption of the hygroscopic nature of PEO/SF blends which affects the phase change process. The authors pose the marked advantage of FTIR & STXM mapping techniques over conventional methods (SEM, AFM, and DSC) to resolve the co-existence of SF and PEO in different phases. It would be interesting to compare the results of a quantitative algorithm such as PLSR to predict concentration of blend components on the hypercube arising from both FTIR mapping and STXM mapping. An important parameter for comparison of STXM imaging and FTIR imaging is scan time, 1 hour for STXM and 10 minutes for the FTIR, per experiment.

Biopolymers derived from agricultural by-products are another important class of polymers. Blood meal-based thermoplastics, for example, are semi crystalline polymers consisting of clusters of crystalline regions of a-helices and b-sheets distributed throughout a randomly coiled protein structure. Synchrotron FTIR was employed by Bier et al to [43], determine spatial variation of protein secondary structures (alpha helices, beta sheets, random coils, turns) of blood meal and blood meal derived thermoplastics, induced by different processing steps (mixing with additives, extrusion, injection moulding, freeze drying). Novatein thermoplastic protein (NTP) was derived from the blood meal and two sample variants were prepared, NTP only and NTP with an additional plasticiser, triethylene glycol (TEG). Each variant was exposed to the four

different processing steps mentioned earlier, and were either prepared in powder or solid blocks (which required 2um thickness microtoming for accurate synchrotron-FTIR readings). Transmission IR spectra were collected in the 3800-800 cm^{-1}range with a 5um spot size. Second derivatives of three peak height ratios were used to analyse spatial distribution of NTP post processing, ratio of absorbance of alpha helix to absorbance of beta sheet(1295-1330 cm^{-1} 1220–1250 cm^{-1}), absorbance of turns to absorbance of beta sheets(1270-1295 cm^{-1}/1220-1250 cm^{-1}), absorbance of random coils to absorbance of beta sheets(1250-1270 cm^{-1}/1220-1250 cm^{-1}), all from the Amide III region (1200-1350 cm^{-1}). The spectra showed both amide I(1600-1700 cm^{-1}) and amide III peaks(1200-1350 cm^{-1}) protein related peaks. However, authors chose amide III peaks for further examination because they offer two advantages: firstly, higher sensitivity to structural changes, and secondly, the ability to resolve overlapping urea and beta sheet absorption bands. Spatial maps of TEG distribution were constructed by comparing the area ratio of the peak at 1040–1090 cm^{-1}(C-OH stretch) to the total area of the amide III region. Peak selection was done as per prior literature review, while peak height ratios were chosen to correct for any difference in thickness of samples. Spatial maps suggested that the additives used to process blood meal into a thermoplastic caused structural rearrangement implying cysteine–cysteine crosslinking between protein chains was disrupted and chain mobility had increased. Extrusion caused drastic structural rearrangement, resulting in a more uniform structure implying consolidation had occurred. In blood meal particles, beta sheets were concentrated around the perimeter of particles, while in extruded and injection moulded materials, beta sheet rich regions were distributed evenly throughout a more disordered matrix. Including TEG as a plasticizer reduced alpha helices and beta sheets and increased the amount of disordered protein chains at

each processing stage. This study demonstrated how FT-IR imaging can be used to characterize the distribution of plasticizers in biopolymers and their fate at high temperatures.

CONCLUSIONS & FUTURE PERSPECTIVES

In this study, we have briefly outlined vibrational spectroscopic chemical imaging techniques, their usage and limitations for polymer characterization. Non-destructive spectroscopic methods for point spectrometric analysis was compared to spatial imaging capabilities of chemical imaging systems and the advantages of this methodology coupled with multivariate analyses were highlighted (e.g. coating homogeneity, crystallinity distribution, visualisation of components of pharmaceuticals).

In many of the papers reviewed, information on coating distribution, uniformity, thickness was missing, which in our opinion, is critical to create a full picture of polymer properties, which in turn influences a system's behaviour. Thickness measurements of a sample should be commonplace, and can be made using direct (e.g. digital micrometers, ellipsometry, AFM) and indirect or derived (e.g. reflectance derived spectroscopy), measurement methods. This would be useful for making comparisons between different analytical techniques(for example, AFM derived thickness data fitted to FTIR reflectance)[21]. In the case of depth profiling, it is important that achievable penetration depths of the selected chemical imaging technique matches the thickness of the surface being analysed[20],[23]. In the future, new research areas in chemical imaging are expected to emerge and some focus areas are detailed subsequently. Methods/techniques required to overcome diffraction limit of systems (appearance of hybrid systems such as AFM/IR or AFM/Raman, Tip Enhanced Raman Mapping, and super-resolution imaging) as well as the standardisation of such systems are expected in the future because this

could bring together, the spatial non-destructive sensing abilities of powerful spectroscopic systems, and the ability to resolve spatial resolution down to the nanoscale, which improves sensing precision for features of interest [21][4].

The presence of overlapping peaks can hinder correct analysis of samples and create ambiguity. There are cases of characterization, using techniques such as XPS (phosphorus related bands overlap[20]) and Raman microscopy (C-H bands[8]) where overlapping peaks present a drawback. Multivariate or Chemometric methods can remedy this situation, as seen in [9], as well as hardware advances such as the optimization of spectral widths of pulses, for time resolved CARS studies[8].

Emphasis on non-destructive depth profiling as opposed to destructive depth profiling studies to characterizethe nature and degree of degradation as well as the ability to carry out accurate depth profiling measurements is required for studying polymers in their native state. Many state of the art depth profiling techniques such as ToF-SIMS are destructive in nature[44]. Non-destructive techniques such as SSPA/FTIR, but with higher spatial and depth resolution are a good alternative[26]. Standardisation of chemometric techniques, decrease in data processing time, better file handling capabilities of systems to increase throughput and efficiency for handling large datasets are expected to improve chemical image analysis. Combining data from complementary chemical imaging modalities is a challenge for data fusion. Selecting the right analytical techniques according to sample specifications is critical to achieve desired selectivity and sensitivity to the sample.

AUTHOR INFORMATION

Corresponding Author

Sindhuraj Mukherjee

sindhuraj.mukherjee@ucdconnect.ie

sindhuraj.mukherjee@gmail.com

Aoife Gowen

aoife.gowen@ucd.ie

Present Addresses

School of Biosystems Engineering, University College Dublin, Belfield, Dublin 4, Co. Dublin, Ireland

Author Contributions

The manuscript was written through contributions of all authors. All authors have given approval to the final version of the manuscript.

ACKNOWLEDGMENT

The authors acknowledge funding from the EU FP7 under the European Research Council Starting Grant programme.

REFERENCES

[1] A. Dazzi, J. Saunier, K. Kjoller, N. Yagoubi, Resonance enhanced AFM-IR: A new powerful way to characterize blooming on polymers used in medical devices, International Journal of Pharmaceutics, 484, (2015),109-114

[2] F. Huth, A. Govyadinov, S. Amarie, W. Nuansing, F. Keilmann, R. Hillenbrand, Nano-FTIR absorption spectroscopy of molecular fingerprints at 20 nm spatial resolution., Nano Lett. 12 (2012) 3973–8

[3] N. Jing, X. Jiang, Q. Wang, Y. Tang, P. Zhang, Attenuated total reflectance/Fourier transform infrared (ATR/FTIR) mapping coupled with principal component analysis for the study of in vitro degradation of porous polylactide/hydroxyapatite composite material, Anal. Methods. 6 (2014) 5590-5

[4] G.L. Warren, L. Sun, V.G. Hadjiev, D. Davis, D. Lagoudas, H.-J. Sue, B-staged epoxy/single-walled carbon nanotube nanocomposite thin films for composite reinforcement, J. Appl. Polym. Sci. 112 (2009) 290–298

[5] R. Gosselin, D. Rodrigue, C. Duchesne, On-line prediction of crystallinity spatial distribution across polymer films using NIR spectral imaging and chemometrics methods, Can. J. Chem. Eng. 86 (2008) 869–878

[6] T. Ishikawa, F. Nishii, H. Mizuno, S.G. Sato, Y. Kazarian, D. Ozaki, Potential of a Newly Developed High-Speed Near-Infrared (NIR) Camera (Compovision) in Polymer Industrial Analyses: Monitoring Crystallinity and Crystal Evolution of Polylactic Acid (PLA) and Concentration of PLA in PLA/Poly-(R)-3-Hydroxybutyrate, Appl. Spectrosc. 67 (2013) 1441-1446

, [7] Y.J. Lee, D. Moon, K.B. Migler, M.T. Cicerone, Quantitative image analysis of broadband CARS hyperspectral images of polymer blends, Anal. Chem. 83 (2011) 2733–2739.

[8] A. Kotiaho, P. Myllyperkiö, M. Pettersson, Chemically selective imaging of overlapping C-H stretching vibrations with time-resolved coherent anti-stokes Raman scattering (CARS) microscopy., J. Phys. Chem. B. 118 (2014) 4363–9

[9] A. Oprea, M. Nistor, L. Profire, M.I. Popa, C.E. Lupusoru, C. Vasile, Evaluation of the Controlled Release Ability of Theophylline from Xanthan / Chondroitin Sulfate Hydrogels, 2013 (2013) 123–131.

[10] L.E. Nita, A.P. Chiriac, M. Nistor, T. Budtova, Upon the Delivery Properties of a Polymeric System Based on Poly(2-Hydroxyethyl Methacrylate) Prepared with Protective Colloids, J. Biomater. Nanobiotechnol. 04 (2013) 357–364.

[11] T. Awatani, H. Midorikawa, N. Kojima, J. Ye, C. Marcott, Morphology of water transport channels and hydrophobic clusters in Nafion from high spatial resolution AFM-IR spectroscopy and imaging, Electrochem. Commun. 30 (2013) 5–8.

[12] L. Sawyer, D. Grubb, G.F. Meyers, Polymer Microscopy, Third Edition, Springer New York, New York, 2008

[13] S.G. Kazarian, K.L.A. Chan, ATR-FTIR spectroscopic imaging: recent advances and applications to biological systems., Analyst. 138 (2013) 1940–51.

[14] S. Sasic, Y. Ozaki, Raman, infrared, and near-infrared chemical imaging, 1st Edition, John Wiley & Sons, Hoboken, New Jersey, 2011.

[15] J. Coates, R.A.M. Ed, Interpretation of Infrared Spectra , A Practical Approach Interpretation of Infrared Spectra , A Practical Approach, in: Encycl. Anal. Chem., John Wiley & Sons, Ltd, Chichester, UK, 2000,10815–10837.

[16] F. Allegrini, Chemometrics in Food Chemistry Federico Marini. Elsevier, Hardbound, 512, J. Chemom. 28 (2014) ,64-100 & 117-118

[17] A. Bonifacio, C. Beleites, F. Vittur, E. Marsich, S. Semeraro, S. Paoletti, V. Sergo, Chemical imaging of articular cartilage sections with Raman mapping, employing uni- and multi-variate methods for data analysis., Analyst. 135 (2010) 3193–204.

[18] Y. Wang, M. Gong, S. Yang, K. Nakashima, Y. GongHemocompatibility and fi lm stability improvement of crosslinkable MPC copolymer coated polypropylene hollow fi ber membrane, J. Memb. Sci. 452 (2014) 29–36.

[19] Popelka, J. Kronek, I. Novák, A. Kleinová, M. Mičušík, M. Špírková, Omastová, M Surface modification of low-density polyethylene with poly(2-ethyl-2-oxazoline) using a low-pressure plasma treatment, Vacuum. 100 (2014) 53–56

[20] K.S. Siow, L. Britcher, S. Kumar, H.J. Griesser, Deposition and XPS and FTIR Analysis of Plasma Polymer Coatings Containing Phosphorus, Plasma Process. Polym. 11 (2014) 133–141

[21] S.R. Kane, P.D. Ashby, L. a Pruitt, ATR-FTIR as a thickness measurement technique for hydrated polymer-on-polymer coatings., J. Biomed. Mater. Res. B. Appl. Biomater. 91 (2009) 613–20

[22] R.G.G. Russell, N.B. Watts, F.H. Ebetino, M.J. Rogers, Mechanisms of action of bisphosphonates: similarities and differences and their potential influence on clinical efficacy., Osteoporos. Int. 19 (2008) 733–759

[23] R. Morent, N. De Geyter, C. Leys, L. Gengembre, E. Payen, Comparison between XPS- and FTIR-analysis of plasma-treated polypropylene film surfaces, Surf. Interface Anal. 40 (2008) 597–600

[24] E. Planes, B. Yrieix, C. Bas, L. Flandin, Solar Energy Materials & Solar Cells Chemical degradation of the encapsulation system in fl exible PV panel as revealed by infrared and Raman microscopies, 122 (2014) 15–23.

[25] Y. Voronko, B.S. Chernev, G.C. Eder, Spectroscopic Investigations on Thin Adhesive Layers in Multi-Material Laminates, Appl. Spectrosc. 68 (2014) 584–592.

[26] W.R. Zhang, T.T. Zhu, R. Smith, C. Lowe, A non-destructive study on the degradation of polymer coating II: Modelling of degradation depth profiles, Polym. Test. 31 (2012) 1100–1104.

[27] K.H. Michaelian, Photoacoustic IR Spectroscopy: Instrumentation, Applications and Data Analysis,Second Edition,Revised and Enlarged Edition, John Wiley & Sons,Weinheim, Germany, 2010,35-37

[28] S.A. Shojaee, A. Zandiatashbar, N. Koratkar, D. a. Lucca, Raman spectroscopic imaging of graphene dispersion in polymer composites, Carbon N. Y. 62 (2013) 510–513.

[29] C.M.S. Izumi, M.L. a. Temperini, FT-Raman investigation of biodegradable polymers: Poly(3-hydroxybutyrate) and poly(3-hydroxybutyrate-co-3-hydroxyvalerate), Vib. Spectrosc. 54 (2010) 127–132.

[30] A. Kljun, T. a S. Benians, F. Goubet, F. Meulewaeter, J.P. Knox, R.S. Blackburn, Comparative analysis of crystallinity changes in cellulose I polymers using ATR-FTIR, X-ray diffraction, and carbohydrate-binding module probes., Biomacromolecules. 12 (2011) 4121–6.

[31] H. Shinzawa, M. Nishida, T. Tanaka, W. Kanematsu, Crystalline structure and mechanical property of poly(lactic acid) nanocomposite probed by near-infrared (NIR) hyperspectral imaging, Vib. Spectrosc. 60 (2012) 50–53.

[32] L. Xue, W. Li, G.G. Hoffmann, J.G.P. Goossens, J. Loos, G. De With, High-resolution chemical identification of polymer blend thin films using tip-enhanced Raman mapping, Macromolecules. 44 (2011) 2852–2858.

[33] S. Berweger, M.B. Raschke, Signal limitations in tip-enhanced Raman scattering: the challenge to become a routine analytical technique., Anal. Bioanal. Chem. 396 (2010) 115–123.

[34] Z.-L. Zhang, L. Chen, S.-X. Sheng, M.-T. Sun, H.-R. Zheng, K.-Q. Chen, H.-X. Xu, High-vacuum tip enhanced Raman spectroscopy, Front. Phys. 9 (2013) 17–24.

[35] N. Brun, P. Bourson, S. Margueron, Quantification of rubber in high impact polystyrene by Raman spectroscopy. Comparison of a band fitting method and chemometrics, Vib. Spectrosc. 67 (2013) 55–60.

[36] J. Blacksberg, G.R. Rossman, A. Gleckler, Time-resolved Raman spectroscopy for in situ planetary mineralogy., Appl. Opt. 49 (2010) 4951–62.

[37] A. Bonifacio, V. Sergo, Effects of sample orientation in Raman microspectroscopy of collagen fibers and their impact on the interpretation of the amide III band, Vib. Spectrosc. 53 (2010) 314–317.

[38] G.L. Alexandrino, R.J. Poppi, NIR imaging spectroscopy for quantification of constituents in polymers thin films loaded with paracetamol., Anal. Chim. Acta. 765 (2013) 37–44.

[39] M.C. Breitkreitz, G.P. Sabin, G. Polla, R.J. Poppi, Journal of Pharmaceutical and Biomedical Analysis Characterization of semi-solid Self-Emulsifying Drug Delivery Systems (SEDDS) of atorvastatin calcium by Raman image spectroscopy and chemometrics, 73 (2013) 3–12.

[40] Kuda-Malwathumullage, C. P. S. and Small, G. W. , Determination of moisture content of polyamide 66 directly from combination region near-infrared spectra. J. Appl. Polym. Sci., 131,(2013), 40645

[41] K. Kunimatsu, B. Bae, K. Miyatake, H. Uchida, M. Watanabe, ATR-FTIR study of water in Nafion membrane combined with proton conductivity measurements during hydration/dehydration cycle., J. Phys. Chem. B. 115 (2011) 4315–21.

[42] S. Ling, Z. Qi, B. Watts, Z. Shao, X. Chen, Structural determination of protein-based polymer blends with a promising tool: combination of FTIR and STXM spectroscopic imaging., Phys. Chem. Chem. Phys. 16 (2014) 7741–8.

[43] J.M. Bier, C.J.R. Verbeek, M.C. Lay, Using synchrotron FTIR spectroscopy to determine secondary structure changes and distribution in thermoplastic protein, J. Appl. Polym. Sci. 130 (2013) 359–369.

[44] L. Bernard, J. Heier, W. Paul, H.J. Hug, The SFM/ToF-SIMS combination for advanced chemically-resolved analysis at the nanoscale, Nucl. Instruments Methods Phys. Res. Sect. B Beam Interact. with Mater. Atoms. 339 (2014) 85–90.

[45] T.R. Crompton, Polymer Reference Book, First Edition, iSmithers Rapra Publishing, Shropshire,U.K., 2006.

[46] L. Kailas, B. Nysten, J.-N. Audinot, H.-N. Migeon, P. Bertrand, Multitechnique characterization of thin films of immiscible polymer systems: PS-b-PMMA diblock copolymers and PS-PMMA symmetric blends, Surf. Interface Anal. 37 (2005) 435–443.

[47] M. Unger, C. Hirschmugl, Synchrotron-Based Fourier Transform Infrared Chemical Imaging: Opportunities for Polymer Research, Microsc. Microanal. 18 (2012) 908–909.

[48] M.F. Tompsett, G.F. Amelio, W.J. Bertram, R.R. Buckley, W.J. McNamara, J.C. Mikkelsen, D. A. Sealer, Charge-coupled imaging devices: Experimental results, IEEE Trans. Electron Devices. 18 (1971) 992–996.

[49] C. Bortolini, M. Dong, Synchrotron Radiation Infrared and Raman Spectroscopy for Biomedical Applications, in: A. Méndez-Vilas (Ed.), Microsc. Adv. Sci. Res. Educ., Formatex Research Center, (2014) 545–556.

[50] E. Levenson, P. Lerch, M.C. Martin, Spatial resolution limits for synchrotron-based spectromicroscopy in the mid- and near-infrared., J. Synchrotron Radiat. 15 (2008) 323–328.

[51] K.P. Knutsen, J.C. Johnson, a. E. Miller, P.B. Petersen, R.J. Saykally, High spectral resolution multiplex CARS spectroscopy using chirped pulses, Chem. Phys. Lett. 387 (2004) 436–441.

[52] W.R. Zhang, T.T. Zhu, R. Smith, C. Lowe, A non-destructive study on the degradation of polymer coating I: Step-scan photoacoustic FTIR and confocal Raman microscopy depth profiling, Polym. Test. 31 (2012) 855–863.

[53] S. Vasiliu, B. Kampe, F. Theil, B. Dietzek, D. Döhler, P. Michael, WH Binder, J Popp, Insights into the mechanism of polymer coating self-healing using Raman spectroscopy., Appl. Spectrosc. 68 (2014) 541–8.

[54] F. Mustata, N. Tudorachi, D. Rosu, Curing and thermal behavior of resin matrix for composites based on epoxidized soybean oil/diglycidyl ether of bisphenol A, Compos. Part B Eng. 42 (2011) 1803–1812.

[55] H. Shinzawa, M. Nishida, T. Tanaka, W. Kanematsu, Accelerated Weathering-Induced Degradation of Poly(Lactic Acid) Fiber Studied by Near-Infrared (NIR) Hyperspectral Imaging, Appl. Spectrosc. 66 (2012) 470–474.

TABLE OF CONTENTS

2. Applications of chemical imaging in polymer characterization

2.1 Surface Characterization

2.1.1 Coating characterization

2.1.2 Plasma polymerization coating studies

2.1.3 Coating Degradation

2.2 Phase distribution in multi-material polymer blends

2.2.1 Graphene and Single Walled Carbon Nanotubes (SWCNT) embedded in polymers

2.2.2 Crystallinity

2.3 Composition based studies

2.3.1 Characterization of pharmaceutical polymers

2.3.2 Moisture content

2.3.3 Protein conformation on polymer surface

3. CONCLUSIONS AND FUTURE PERSPECTIVES

4. ACKNOWLEDGEMENTS

5. REFERENCES

Characterization Method	Property Investigated	Nature of analysis
Gel Permeation Chromatography(GPC)[45]	Mass analysis : Number average molecular mass, molecular mass distribution	Destructive for sample
Mass Spectroscopy(MS)[45]	Structural and functional group analysis : identification of chemical moieties and conformational state	Destructive for sample
X-Ray Diffraction(XRD)[30]	Structural and functional group analysis, degree of crystallinity.	Destructivity depends on sample preparation method used

Nuclear Magnetic Resonance(NMR)[29]	Structural and functional group analysis, identification of exact structure, chemical moieties, and conformational state	Laborious sample preparation, non-destructive
Small Angle X-ray scattering(SAXS)[45]	Microscopic domain analysis	Minimum sample preparation, non-destructive
Electron Microscopy (Scanning, Transmission) : SEM, TEM[3]	Microscopic domain analysis	Laborious sample preparation, destructive for sample
Atomic Force Microscopy(AFM)[21]	Measures physical surface	Laborious sample preparation, destructive for sample

	characteristics such as roughness	
Transmission Optical Microscopy[28]	Structural analysis	Requires transparent samples
Differential Scanning Calorimetry(DSC)[40]	Determines phase transition, melting point, reaction kinetics of polymers	Destructive for sample
Thermogravimetric Analysis (TGA)[40]	Determines thermal degradation pathway of polymers	Destructive for sample
Dynamic Mechanical Analysis (DMA)[45]	Mechanical analysis(tensile strength, Young's Modulus)	Destructive for sample

Viscometry[45]	Mechanical analysis(tensile strength, Young's Modulus)	Destructive for sample
Thermomechanical Analysis (TMA)[31]	Thermo-mechanical behaviour	Destructive for sample
X-Ray Photoelectron Spectroscopy(XPS)[46]	Structural and functional group analysis	Requires Vacuum, destructive for sample

Table 1: Traditional Methods of Polymer Characterization

Characteristic shift / Peak	Bond type/Chemical Species type	Polymer	Modality
1002 cm^{-1}	Phenyl ring stretch	Poly(styrene-co-acrylonitrile) (SAN)	Tip Enhanced Raman Spectroscopy[32]
1013-1000 cm^{-1}	*va*(P-O-P)	Poly PO_4 arising from diethyl phosphite and triisopropylphosphite	ATR-FTIR[22]
1017 cm^{-1}	C-O-C	Ethyl Vinyl Acetate (EVA)	ATR-FTIR[30]
1025 cm^{-1}	*v*(P=O)	Hydroxyapatite	ATR-FTIR[3]
1039 cm^{-1}	*v*(C=O)	diethyl phosphite	ATR-FTIR[22]
1095 cm^{-1}	C-O	Ethyl tetraflouroethylene (ETFE)	ATR-FTIR[30]
1115 cm^{-1}	C-O	Ultra high molecular weight polyethylene	ATR-FTIR[23]
1140 cm^{-1}	*yr*(CH_3)	Triisopropylphosphite	ATR-FTIR[22]
1145 cm^{-1}	δCH_2	Poly methyl methacrylate	s-SNOM[2]
1165 and 1040 cm^{-1}	C-F bond	Ethyltetraflouroethylene	Raman[30]
1184-1000 cm^{-1}	*v*(C=O)	Polyethylene oxide (PEO)	FTIR[42]
1190 cm^{-1}	$\delta C{-}O{-}C$	Poly methyl methacrylate	s-SNOM[2]
1220 cm^{-1}	*v*(P=O)	Poly PO_4 arising from diethyl phosphite and triisopropylphosphite	ATR-FTIR[22]
1236 cm^{-1}	C-O	Ethyl Vinyl Acetate (EVA)	ATR-FTIR[30]
1240 cm^{-1}	*va*(O-P=O)	2-Methacryloyloxyethyl phosphorylcholine	ATR-FTIR[19]
1250-1220 cm^{-1}	Amide III Beta sheet	Novatein thermoplastic protein	Synchrotron-FTIR[43]

1265 cm^{-1} and 1240 cm^{-1}	***δ*C−C−O**	**Poly methyl methacrylate**	**s-SNOM[2]**
1270-1250 cm^{-1}	**Amide III Random coil**	**Novatein thermoplastic protein**	**Synchrotron-FTIR**[43]
1295-1270 cm^{-1}	**Amide III Random turns**	**Novatein thermoplastic protein**	**Synchrotron-FTIR**[43]
1330-1295 cm^{-1}	**Amide III Alpha helix**	**Novatein thermoplastic protein**	**Synchrotron-FTIR**[43]
1370 cm^{-1}	***δs*(CH_3)**	**Triisopropylphosphite**	**ATR-FTIR[22]**
1380 cm^{-1}	***δa*(CH_3)**	**Triisopropylphosphite**	**ATR-FTIR[22]**
1430 cm^{-1}	**Cellulose I**	**Cotton fibres**	**ATR-FTIR**[30]
1440 cm^{-1}	**triazole ring symmetric stretch**	**Triazole ring on poly(isobutylene) alkyne**	**Raman[53]**
1450-1250 cm^{-1}	**D band (graphene platelets) ; breathing modes of six-atom rings**	**Bisphenol A epoxy resin**	**Confocal Raman Microscopy**[28]
1500-1700 cm^{-1}	**G band (graphene platelets) : doubly degenerate phonon mode**	**Bisphenol A epoxy resin**	**Confocal Raman Microscopy**[28]
1560 cm^{-1}	**νC–N + δN–H**	**ethylene bisstereamide (EBS)**	**AFM-IR[1]**
1590-1580 cm^{-1}	**G-band , Single Walled Carbon Nanotube (SWCNTs)**	**Epoxy resin**	**Confocal Raman Microscopy[4]**
1600-1500 cm^{-1}	**Silk fibroin (Amide II) bands**	**Silk fibroin**	**FTIR**[42]
1630 cm^{-1}	**NCO-**	**Poly(2-ethyl-2-oxazoline)**	**ATR-FTIR[20]**
1634 cm^{-1}	**νC=O**	**ethylene bisstereamide (EBS)**	**AFM-IR[1]**
1644 cm^{-1}	***ν*(C=C) of 1,2-vinyl**	**Polybutadiene in polystyrene**	**Raman spectroscopy**[35]
1656 cm^{-1}	**C=C stretch of 1,4 cis**	**Polybutadiene in polystyrene**	**Raman spectroscopy**[35]
1671 cm^{-1}	**C=C stretch of 1.4 trans**	**Polybutadiene in polystyrene**	**Raman spectroscopy**[35]
1680 cm^{-1}	**O=P-OH bond, OH deformation**	**Triisopropylphosphite**	**ATR-FTIR[22]**
1720, 1670 cm^{-1}	**1,3-dimethyl-7H-purine-2,6-dione**	**Theophylline**	**ATR-FTIR[9]**
1725 cm^{-1}	***ν*(C=O)**	**Polyhydroxybutyrate (PHB)**	**Fourier Transfer-Raman spectroscopy**[29]
1730cm^{-1}	**νC=O**	**Poly methyl methacrylate**	**s-SNOM[2]**

1733 cm^{-1}	***v*(C=O)**	**Ethyl Vinyl Acetate (EVA)**	**ATR-FTIR[30]**
1738 cm^{-1}	**C=O bond**	**polypropylene**	**ATR-FTIR[25]**
1738 cm^{-1}	**C=O bond**	**Ethyl tetraflouroethylene (ETFE)**	**ATR-FTIR[30]**
1750 cm^{-1}	**C=O stretch**	**2-Methacryloyloxyethyl phosphorylcholine**	**ATR-FTIR[19]**
1755 cm^{-1}	**C=O bond**	**Poly-L-Lactic acid (PLLA)**	**ATR-FTIR[3]**
2125 cm^{-1}	***v*(C≡C)**	**poly(isobutylene) alkyne**	**Raman[53]**
2800-2600 cm^{-1}	**2D band (graphene platelets) : D band overtone**	**Bisphenol A epoxy resin**	**Confocal Raman Microscopy**[28]
3211 cm^{-1}	**Free νO-H or [H3O+(H2O)] hydronium ion**	**Nafion**	**AFM-IR[11]**
3482 cm^{-1}	**Bound νO-H**	**Nafion**	**AFM-IR[11]**
787 cm^{-1}	**P-O-C**	**diethyl phosphite**	**ATR-FTIR[22]**
800 cm^{-1}	***v*(C-C)**	**Poly(methyl) methacrylate (PMMA)**	**Tip Enhanced Raman Spectroscopy**[32]
843-825cm^{-1}	**Epoxy ring**	**Epoxidised soybean oil**	**FTIR[54]**
893 cm^{-1}	**Cellulose II**	**Cotton fibres**	**ATR-FTIR**[30]
961 cm^{-1}	***v*(C-C)**	**Diethyl phosphite**	**ATR-FTIR[22]**

Table 2: Peak Assignment for vibrational and rotational frequencies of chemical species from Infrared & Raman spectra, where, *v* = stretch, *a* = asymmetric. *s* = symmetric, δ = bend, *yr*= rocking vibration

Infrared Chemical Imaging Technique	**Description**

Fourier Transform Infrared (FTIR) [42]	• Earlier systems collect spectra from sample, subject to different λ of IR light one by one • Interferometer : scans all λ simultaneously, contains beamsplitter • Beamsplitter : IR source hits beamsplitter, splits IR light into two beams : first beam simply bounces of a fixed flat mirror, and the second beam, reflects off a mobile flat mirror. • mobile flat mirror moves a very slight distance away from the beamsplitter, which results in interference patterns, when the two beams recombine • Recombination of the two beams contains data which is a function of the distance moved by the mobile mirror, representative of the entire frequency spectrum coming from the source of the infrared beam. A Fourier Transform is then applied to each interferometer signal to get frequency spectra. This forms the basis for a Fourier Transform Infrared Spectrometer (FTIR). • For imaging systems, sample stage is simply raster scanned and the spectra for each point on the sample are collected as an image. . • Point scan systems replaced by 2-D Focal plane array (FPA) or linear arrays (e.gHgCdTe ,InGaAs photodiodes)[12] or charged couple devices. Spectral scanning is done in

	transmission or reflectance mode.
Attenuated Total Reflectance-Fourier Transform Infrared imaging (ATR-FTIR)[21]	• Polished crystal surface (e.g., diamond, germanium) contacts the sample surface • IR light passes through the crystal, generates an evanescent wave through the sample[12]. • Wave gets attenuated – function of material properties • linear or a focal plane array detector is then used to detect the response
Synchrotron Fourier Transform Infrared	

Spectroscopy[47]	• Synchrotron light source is used to provide a very bright spectrum, resulting in an improvement of the signal to noise ratio.
Atomic Force Microscope – Infrared Imaging (AFM-IR)[1]	• Sample is irradiated with pulses of infrared radiation ; using the tip of an AFM absorbed radiation with nanoscale spatial resolution is detected • IR light absorbed by the sample is converted to heat, causing a rapid thermal expansion pulse under the AFM tip, in turn exciting resonant oscillation of the AFM cantilever • Amplitude of the cantilever oscillation is directly proportional to the sample absorption coefficient, thus AFM-IR absorption spectra generated by measuring the cantilever oscillation amplitude as a function of the wavelength of the incident radiation
Scattering type Scanning Near-filed optical	• Metallized AFM tip is used to enhance and scatter radiation from a nanometer scale region

Microscope (s-SNOM)[2]	of the sample • Optical amplitude and phase of the scattered light can be measured, converted into measurements of the complex optical constants of the material under the tip
Raman Chemical Imaging Technique	**Description**
Raman Microscopy	• Section of polymer sample is irradiated by a laser (excitation wavelength is typically in the VIS or NIR). Rayleigh rejection filters remove elastically scattered light from the sample • Sample is typically moved under the laser beam to gather Raman scatter over a defined area. Raman scatter is detected by a CCD(charge couple device) [48]), and a spectrum of Raman shifts versus intensity unit is generated through which Raman shifts are analyzed.

Confocal Raman Microscopy (CRM) [26]	• Confocality refers to the ability to spatially control the analysis volume of the sample, in the XY (lateral) and Z (depth) axes • Signal generation is the same as a conventional Raman microscope.
Tip Enhanced Raman Microscopy(TERM) [32]	• Use of a sub-nanometer tip (e.g gold) as a probe acting as a plasmonic enhancer is placed on sample to provide nanoscale spatial resolution of sample surface structures.The excitation laser light is focused onto the tip-apex to enhance the Raman signal in close proximity to the tip. The lateral resolution is dependent on the tip-apex size (10 – 20 nm). • Correctly integrated probe causes local enhancement of Raman effect on sample, which is detected by a CCD. • Nanoscale structures are more resolved and correctly correlated to the Raman signature of

	the corresponding surface feature
Broadband-Coherent Anti-Stokes Raman Spectroscopy(B-CARS)[7]	• Non-linear microscopy technique, resulting in high Raman signal intensity • Uses difference between two excitation beams, pump & Stokes beams to coherently excite single Raman band • Emission at Anti-Stokes wavelength detected, non-resonant background removed, resulting in high Raman signal intensity
Time Resolved Coherent Anti-Stokes Raman Spectroscopy(TR-CARS)[8]	• This technique is a modification of the coherent anti stokes Raman scattering (CARS) technique using ultra-fast lasers to study a reaction in the time domain.

Table 3: Table outlining major Infrared and Raman modalities compared in this review

Modality	**Advantage**	**Disadvantage**
FTIR	Fast, very little sample preparation	Limited spatial resolution because of diffraction limit. Thick and dense samples such as teeth or bones (natural polymeric systems) difficult to analyze [49]
ATR-FTIR	no sample preparation, pump down, or sputtering [21] allows bulk and surface measurements	Spatial resolution limited by diffraction limit (but better than FTIR)

Synchrotron FTIR	Higher spatial resolution and signal to noise ratio as compared to ATR-FTIR[50]	Synchrotron light sources not available to common laboratories
CRM	No sample preparation good for mineral component resolution, a voids water signal therefore suitable for analyzing biological systems	May induce thermal-damage on sample depending on laser power used, high fluorescence is possible[49]
TERM	Diffraction limit overcome by use of localized plasmonic enhancement resulting in higher Raman signal. [32]	Requires experience in Raman spectroscopy, SPM/AFM microscopy, and resonance enhancement to get accurate measurements, (maximum Raman intensity when the tip was approached or was withdrawn from the sample surface is required for measurements), Enhancement factor is different for different tips used [32]

B-CARS	Higher Signal to Noise Ratio as compared to single band CARS, Stimulated Raman Scattering and conventional Raman Imaging	Complex instrumentation, systems are custom built and can result in low spectral resolution as well as thermal damage to sample if chirped pulses are not used [51]

AFM-IR	Nanoscale spatial resolution	Complex instrumentation, slow acquisition rate, AFM tip & sample interaction needs to be optimized[1]
s-SNOM	Subnanometre resolution	Slow acquisition time[2]
Tr-CARS	High chemical specificity of single molecule vibration[8]	Highly complex instrumentation, and difficult to operate, requires synchronicity of lasers[8]

Table 4 : Table listing the advantages and disadvantages of different techniques

NON SPATIAL ANALYSIS					

MODALITY	SAMPLE MATRIX	ENTITY TRACKED	INVESTIGATION	CHEMOMETRIC TECHNIQUE	REFERENCE
ATR FTIR	Polypropylene hollow fibre membrane	(2-methacryloyloxyethyl phosphorylcholine-co-n-butyl methacrylate- co-3-(Tri-methoxysilyl) propyl methacrylate) (PMBT) coating	PMBT coating	Peak fitting	Wang et al 2014[18]
ATR-FTIR	ZnSe crystal	TIP,DEP,1,7-octadiene copolymers	polyphosphate formation on	Peak fitting	Siow et al 2014[20]

			polymer		
ATR FTIR,	Ultra High Molecular Weight Polyethylene (UHMWPE)	Tetraglyme coating	Thickness prediction	Peak area	Kane et al 2009[21]
Confocal Raman microscopy	Aliphatic polyester resin	Melamine crosslinked coating	Coating degradation	Peak area	Zhang et al 2012a[52]
Confocal Raman microscopy	Aliphatic polyester resin	Melamine crosslinked coating	Coating degradation & modelling	Peak area, logistic function	Zhang et al 2012b[26]

Raman spectroscopy	Polyisobutylene network	Triazole ring	Qualitative analysis of polymer self-healing	None	Vasiliu et al 2014[53]
Fourier Transform Raman spectroscopy	Poly-R-3-hydroxy butyrate (PHB) & poly[(R)-3-hydroxybutyrate-co-(R)-3-hydroxyvalerate (PHBV)	1725 cm^{-1} (C=O bond) of PHB,PHBV	Change in crystallinity on change of temperature	Peak fitting	Izumi &Temperini 2010[29]
ATR-FTIR	Cotton fibres	Cellulose I, Cellulose II crystal forms	Change in crystallinity on NaOH treatment	Peak fitting	Kljun et al 2011[30]

FTIR transmission	Polyamide 66	Moisture	Moisture content prediction	None	Kuda-Malwathumullage and Small 2014[40]
SPATIAL ANALYSIS					
MODALITY	SAMPLE MATRIX	ENTITY TRACKED	INVESTIGATION	CHEMOMETRIC TECHNIQUE(S)	REFERENCE

ATR-FTIR MIR imaging	Photovoltaic module encapsulant (10 layers) :Ethyl Tetra Flouro Ethylene (ETFE), Ethyl Vinyl Acetate (EVA), Poly Ethylene Terepthalate (PET)	Encapsulant : EVA, PET	Degradation of encapsulant& other layers ; UV, accelerated ageing 80 deg C/85% relative humidity for 2000hours	PCA	Planes 2014[24]
ATR-FTIR MIR imaging	Sample 1 = polyethylene terephthalate (PET) + polyvinyl fluoride(PVF), Sample 2 = polyethylene terephthalate (PET) + polyvinyldiene fluoride (PVDF) ; PVF, PVDF = outer layers ; adhesive present between outer layers,	Adhesive	Degradation of adhesive layer : UV 0.72W/m^2 , 340nm ; Xe weathering (simulated solar light spectrum);		Voronko 2014[25]

	core and backsheet		80/85%relative humidity;80-85 deg C; 0.5%NH_3 in N_2		
ATR-FTIR MIR imaging	Poly-L-Lactic Acid (PLLA)/Hydroxyapatite(HA) blend created by solvent casting	PLLA	Degradation of PLLA/HA blend in Phosphate Buffer Saline Solution over 7 day intervals from day 0 to day 105		Jing 2014[3]
Confocal Raman	Bisphenol A epoxy resin	Filler: Graphene Platelets (GPLs) fillers (0.05%, 0.1 %, 0.2%, 0.03%,	Phase dispersion and agglomeration	peak area for carbon	Shojaee 2014[28]

Imaging		0.04%)	of GPLs in blend	related bands	
Confocal Raman Imaging	B stage epoxy resin	Filler : Single Wall Carbon Nanotubes (SWCNTs) : native form, oxidised SWCNTs, functionalised SWCNTs	Phase dispersion and morphology of different CNTs in blends linked to thermo-mechanical behaviour		Warren 2009[4]
NIR Imaging	Diglycidyl Ether of Bisphenol-A(DGEBA) resin cured with p-amino benzoic acid	Filler: epoxidised soybean oil or ESO (5%, 10%, 15%)	Distribution of ESO in blend linked to thermo-mechanical	PLS-DA	Mustata 2011[54]

			analysis		
NIR Imaging	Poly-L-Lactic Acid (PLLA) pellets 0.2mm	Filler : Organic clay particles (montmorillonite) ; 0%, 5%, 15%	Variation of crystalline structure of PLLA on addition of clay linked to thermo-mechanical analysis		Shinzawa 2012[55]

NIR Imaging	Poly-L-Lactic Acid(PLLA)/Poly-R-3-Hydroxybutyrate(PHB) thin film (0.2-0.7mm thickness), six blend ratios : 100/0,80/20,60/40,40/60,20/80,0/100	Constituent : PLLA	Crystallinity of blend constituents using heating temperature slope(70-105deg C)	PLS Regression	Ishikawa 2013[6]
Raman Mapping	Polystyrene	Filler : Polybutadiene(rubber) : 0 to 10%	Quantification of polybutadiene	PCA, PLSR	Brun 2013[35]
time resolved Coherent Anti Stokes Raman	Polypropylene sheet	3% octamethyl polyhedral oligomericsilsesquioxane (om-POSS)	Investigation of distinction between blend components containing partially	None	Kotiaho 2014[8]

Scattering (tr-CARS) mapping		microparticles	overlapped bands		
NIR Imaging	Xanthum/Chondroitin sulphate hydrogel	Loading drug : theophylline	Drug distribution	PCA, PLS-DA	Oprea 2013[9]
FTIR Imaging	hydroxyl propyl methyl cellulose (HPMC), poly vinyl pyrrolidone (PVP), Poly ethylene glycol (PEG) thin film	Loading drug : paracetamol	Drug quantification	PLS, MCR-ALS	Alexandrino 2013[38]
Raman Imaging	hydrophillic and lipophillic complex blend	Loading drug : Atorvastatin Calcium homegeneity	Drug distribution	PLS	Breitkreitz 2013[39]

NIR Imaging	Thin films of high density polyethylene(HDPE), low density polyethylene(LDPE), polypropylene(PP)	HDPE, LDPE, PP	Crystallinity of each polymer independently	Multiway PCA, PLS, multivariate image regression(MIR)	Gosselin 2008[5]
synchrotron FTIR Imaging	silk fibroin/Poly ethylene oxide	Silk fibroin	Conformation of silk fibroin	K means clustering	Ling 2014[42]
Confocal Raman Microscopy	Articular cartilage tissue	collagen, non-collagen protein, proteoglycans, nucleic acid	Distribution of Extracellular components in	PCA, PLSR, Hierarchical cluster analysis	Bonifacio 2010[17]

			tissue	(HCA), fuzzy cluster analysis (FCA)	
Broadband Coherent Anti Stokes Raman Scattering(B-CARS) Microscopy	Polystyrene(PS)/poly(styrene-ethylene/propylene)(SEP)/Propylene(PP) blend	compatibilizer SEP	Concentration of compatibilizer SEP	Singular Value Decomposition (SVD), Classical Least Squares (CLS)	Lee 2011[7]

Tip Enhanced Raman Mapping (TERM)	poly(methyl methacrylate) (PMMA)/ poly(styrene-co-acrylonitrile) (SAN) 500nm(thickness) thin film	Interphase of the copolymer	Phase transition of PMMA		Xue 2011[32]
synchrotron FTIR Imaging	Novatein thermoplastic protein (NTP), triethylene glycol (TEG)	NTP	Protein secondary structure of NTP and distribution of TEG	None	Bier 2013[43]
Atomic Force Microscopy (AFM-IR)	Polyther-urethane catheter	Irganox 1076as antioxidant, ethylene bisstearamideas a lubricant	Distribution of local deposits of lubricant	None	Dazzi 2015[1]
Atomic Force Microscopy (AFM-IR)	Nafion membrane	Bulk & free water	Localisation of bulk & free water	None	Awatani 2013[11]

Scattering-type scanning near-field optical microscopy (s-SNOM)	Silicon wafer(PDMS)	poly(methyl methacrylate) (PMMA)	Presence or absence of PMMA	None	Huth et al 2012[2]

Table 5:Table summarising all the non-spatial and spatial analyses covered in this review paper

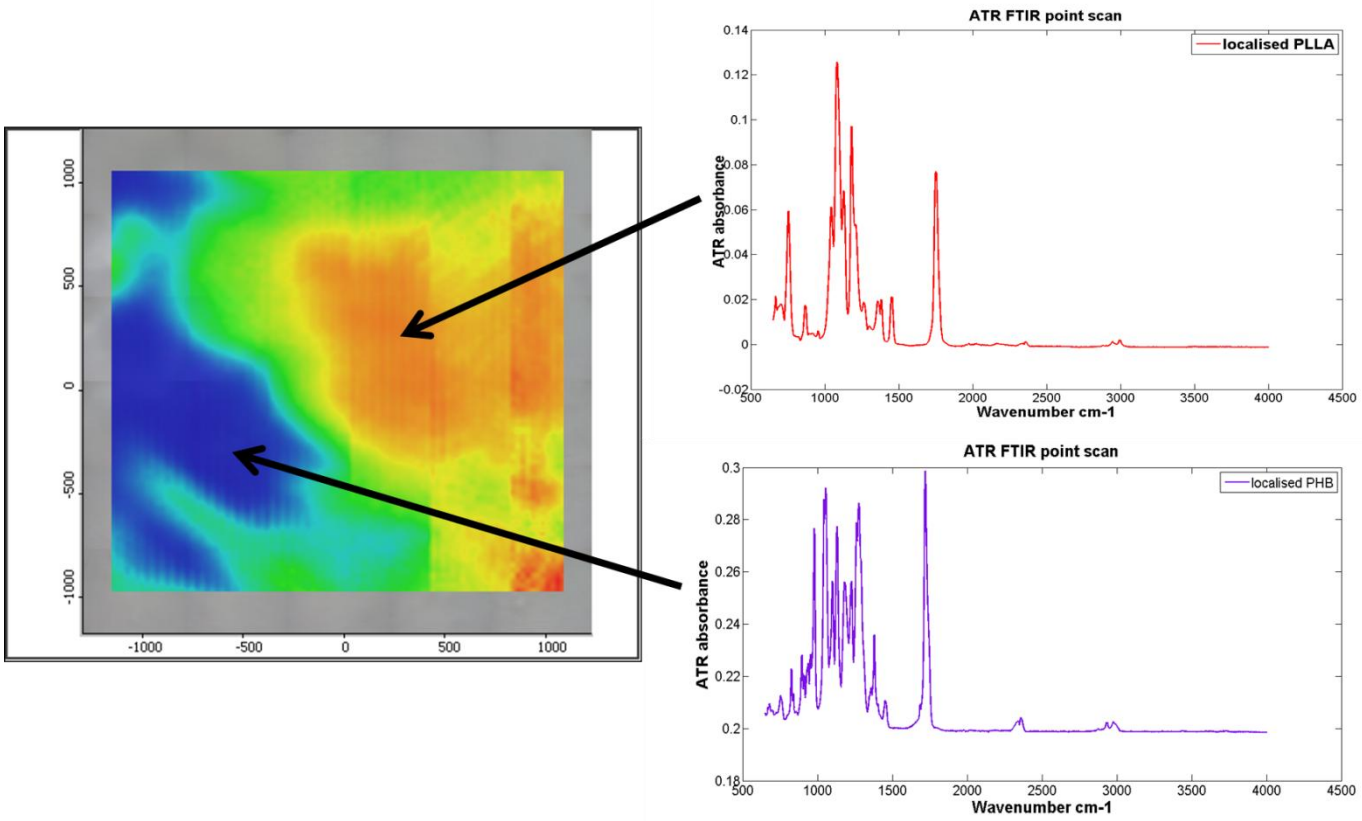

Figure 1: The image shows a false color reflectance based blend distribution image of a PLLA: P3HB 50:50 blend solvent cast film. Yellow/Red sections show the concentration of Poly-L-Lactic acid(PLLA) and the green/blue section shows concentrations of Poly-3-hydroxybutyrate(P3HB) by selecting the 1753cm^{-1} representing the C=O bond(PLLA) and 1720cm^{-1} for the same bond (P3HB) in the blend. This image was taken using air as reference, 4000-800 cm^{-1}range, spectral resolution = 4 cm^{-1}, spatial resolution = 4um

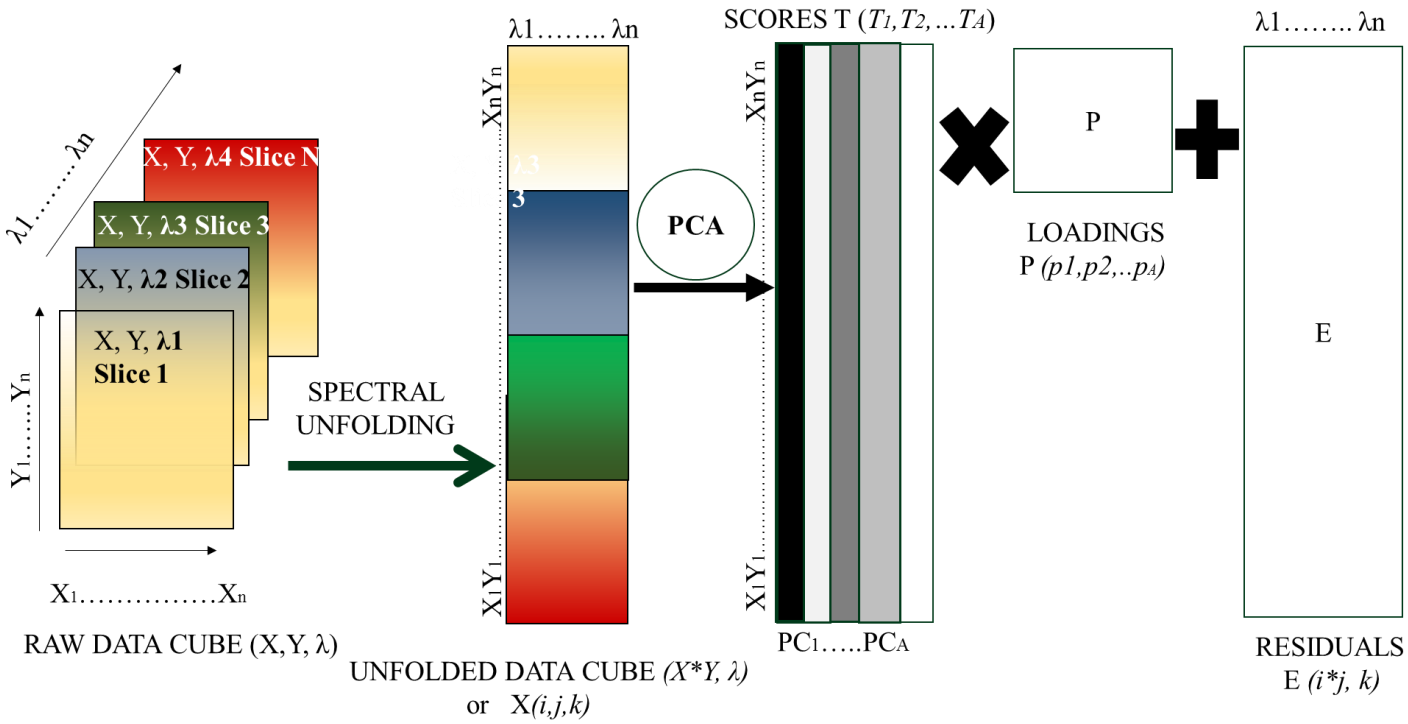

Figure 2 ;Application of Principal Component Analysis(PCA) to a chemical image. First the data cube is unfolded. PCA is applied to the unfolded data cube resulting in scores, loadings and a residual matrix. **λ** = wavelength range of the spectral component ($\lambda_1 \ldots \lambda_n$), X and Y refer to the indices for spatial components, spanning the image scan area (X,Y,**λ**can have values ranging from 1 to n, which are pixel indices for the image).

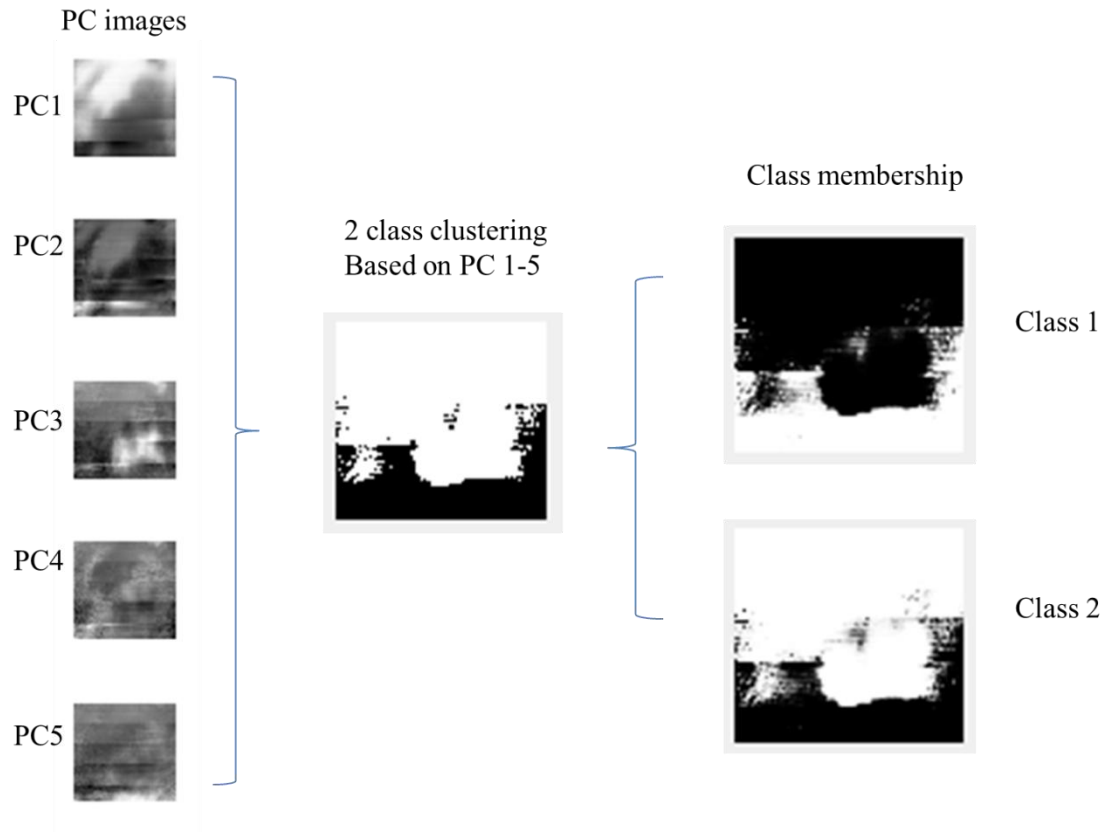

Figure 3 :A chemical image of a polymer blend (PLLA:PHB, 50:50) was subjected to PCA. PC score images (1-5, >99% variance in dataset) were used as inputs to a Gaussian mixture clustering algorithm, with 2 classes. The results of this are shown in the middle section of Fig 3, where black pixels represent Class 1 and white pixels represent Class 2. The class membership (i.e. the posterior probability of a pixel belonging to each class) is shown on the right hand side of Figure 3. This kind of soft classification can be used to identify intermediate pixels belonging to both classes.

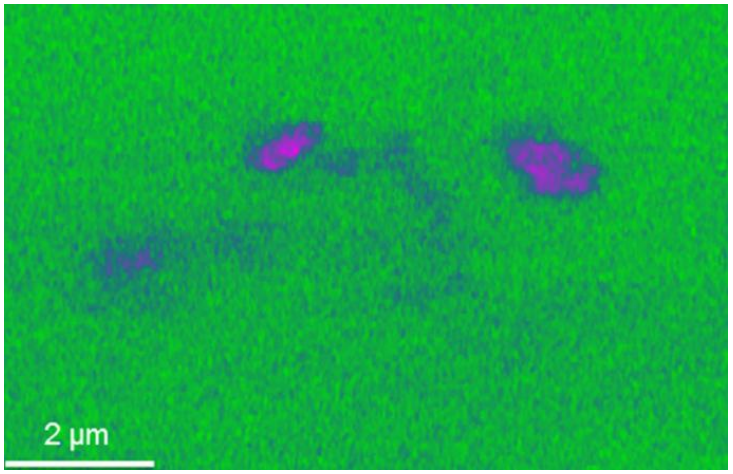

Figure 4 :Image representing the 1634cm-1 band intensity of lubricant in a polyurethane matrix taken using AFM-IR. Image sourced from [1]

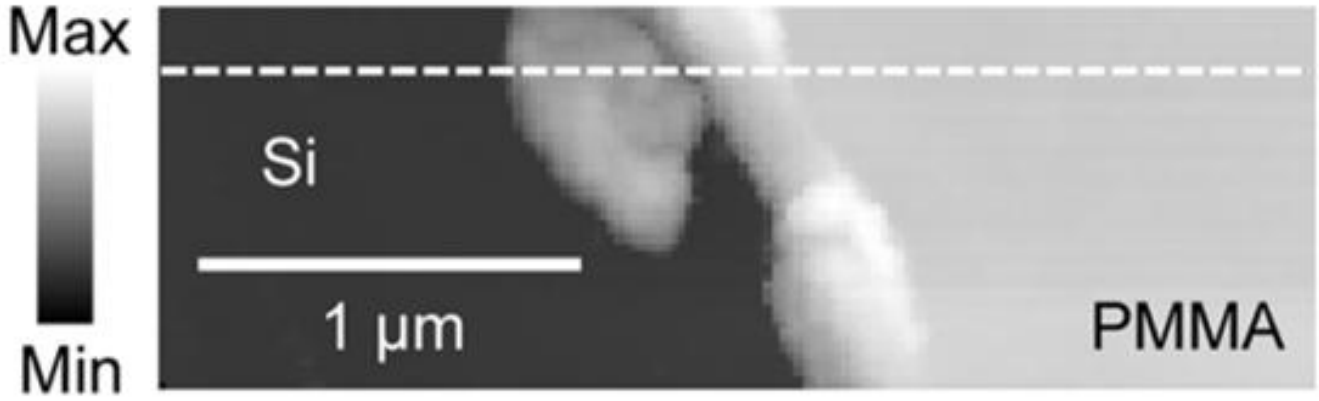

Figure 5 :Infrared nanoimaging of a polymer thin film (PMMA) on a Si substrate. [2]

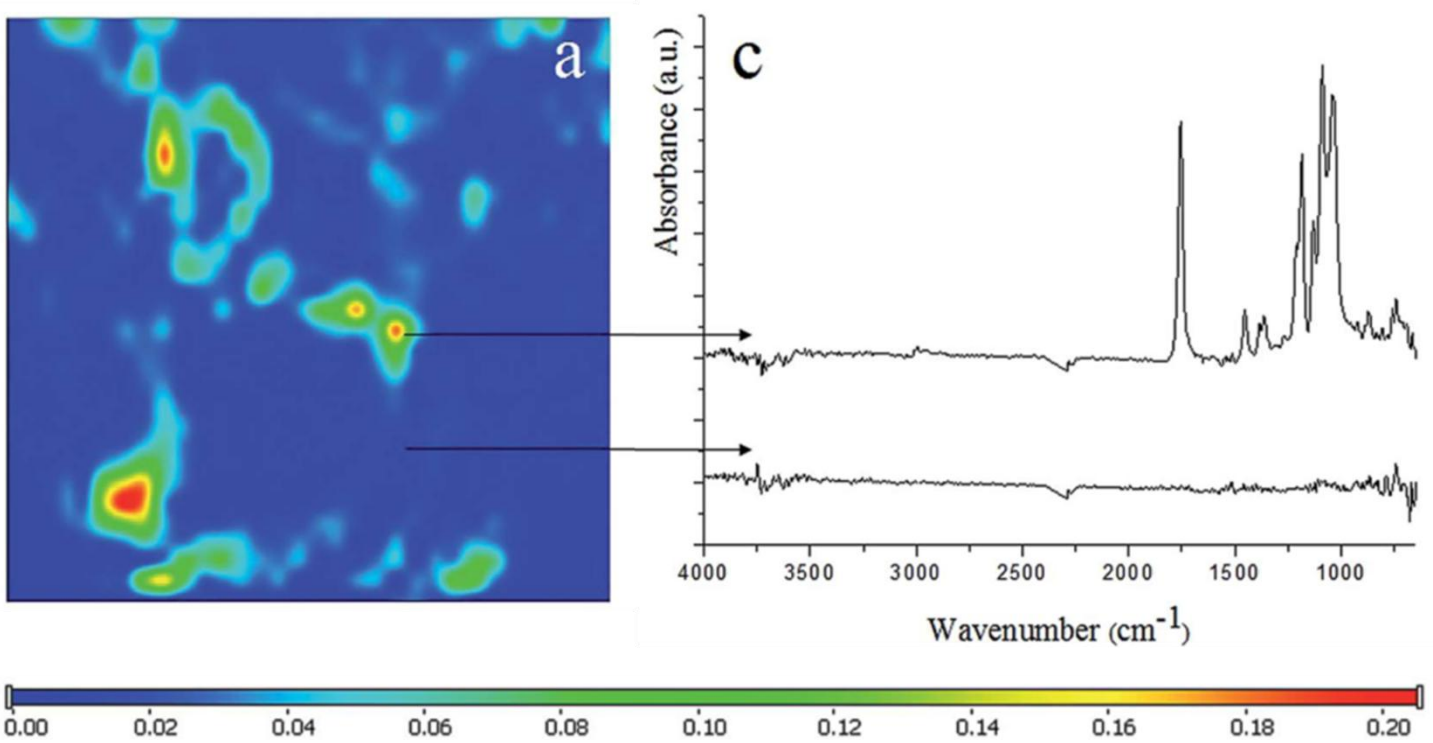

Figure 6 :FTIR image of non-degrading PLLA/HA composite material (a) FTIR image based on the absorption band at 1755cm-1; (b) color scale; and (c) FTIR spectra of different pixels in the image. Image sourced from [3]

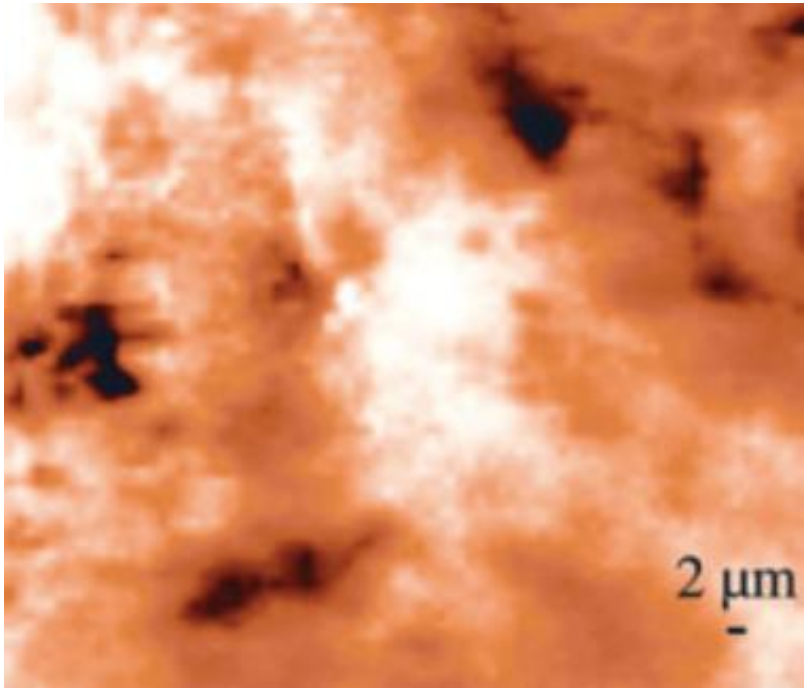

Figure 7 :Orange represents the SWCNT : G-band distribution (black represents high concentration of SWCNT), white represents the epoxy resin distribution. Image sourced from [4]

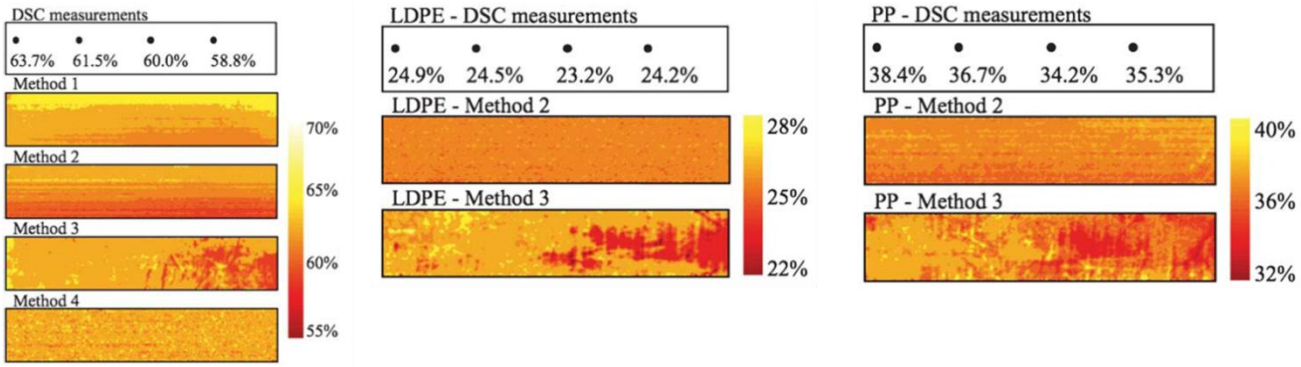

Figure 8: From left to right, predicted crystallinity values of HDPE, LDPE & PP. Predicted crystallinity distribution for HDPE cooled at 4 C/min. Values are given in % crystallinity. Sample size: 100 mm×40 mm. Method 1 uses averaged NIR spectra & PLS regression, Method 2 uses second derivative NIR spectra & PLS regression, Method 3 uses MIA/MIR using raw reflectance spectra, Method 4 uses MIA/MIR using second derivative spectra. Image sourced from [5]

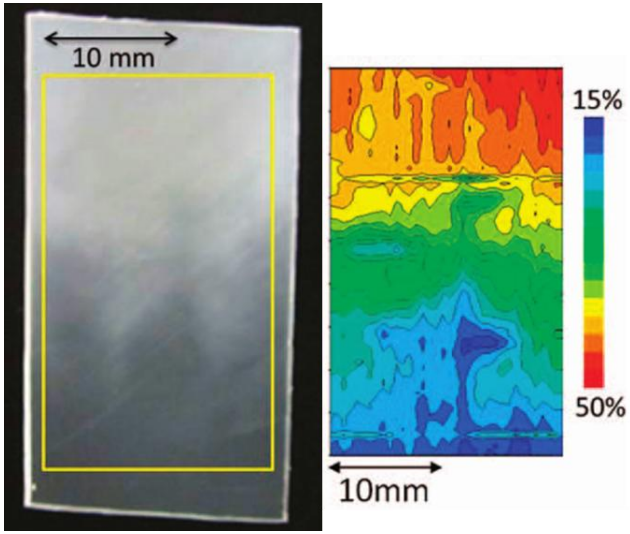

Figure 9 :Optical image of PLLA sample (left), SNV treated spectra of predicted crystallinity of same section (right). PLLA sample kept on hot stage, depict the effect of temperature and crystallinity on the top portion of the image. Image sourced from [6]

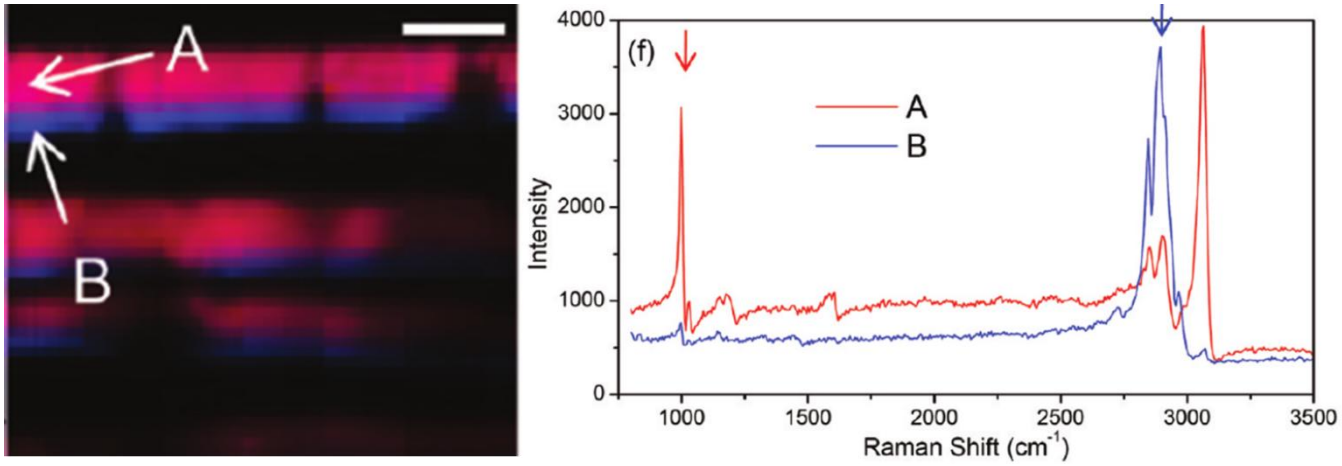

Figure 10 :CARS hyperspectral image of the PS/PP blend. The raw CARS data was used to construct an image (left), where the red and blue color indicates the intensity at 990 and 2880 cm^{-1}, respectively for polystyrene (PS) and polypropylene (PP). Image sourced from [7]

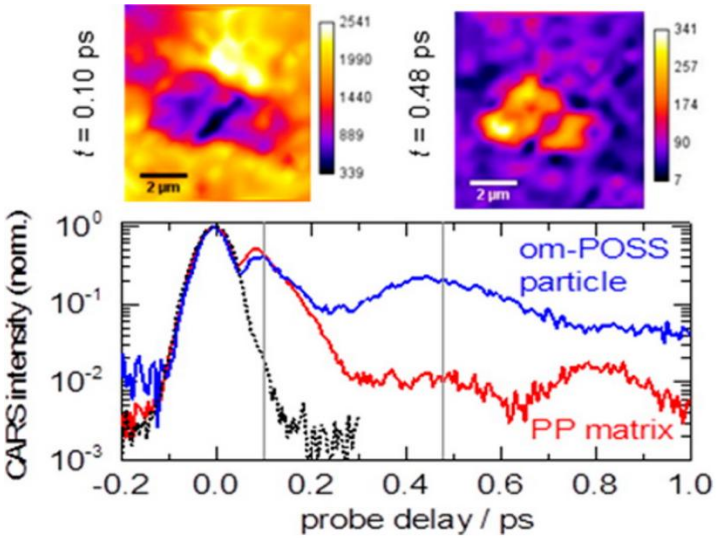

Figure 11 : Chemically selective imaging is demonstrated for composite material of polypropylene (PP) matrix and om-POSS (octamethyl polyhedral oligomericsilsesquioxane) microparticles having partly overlapping CH stretching vibrations. CARS images measured at a probe delay of (A) 0.10 ps and (B) 0.48 ps and (C) image obtained by dividing the CARS intensity at each pixel at 0.48 ps by the intensity at 0.10 ps. (D−F) Profiles of CARS intensities across images A−C, respectively. Image sourced from [8]

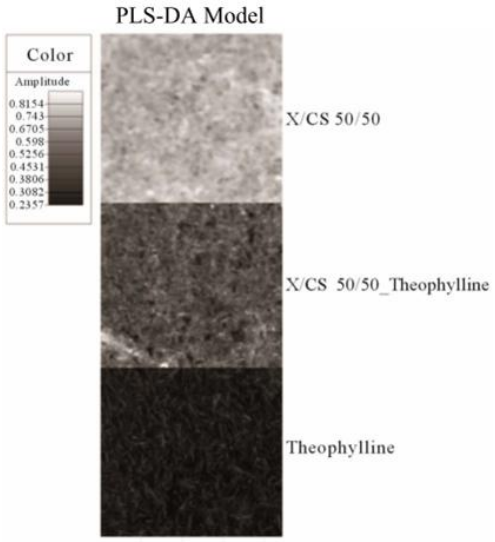

Figure 12 :This figure shows the distribution of different components as predicted by the PLS-DA model. Pure drug theophylline is represented by black, whose distribution can be visualised in the middle picture. Image sourced from [9]

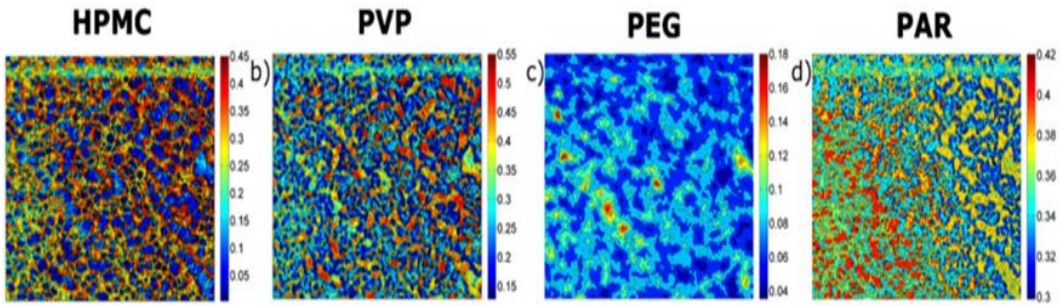

Figure 13 :Concentration maps of HPMC, PVP, PEG and PAR obtained from PLS models. Image sourced from [3]

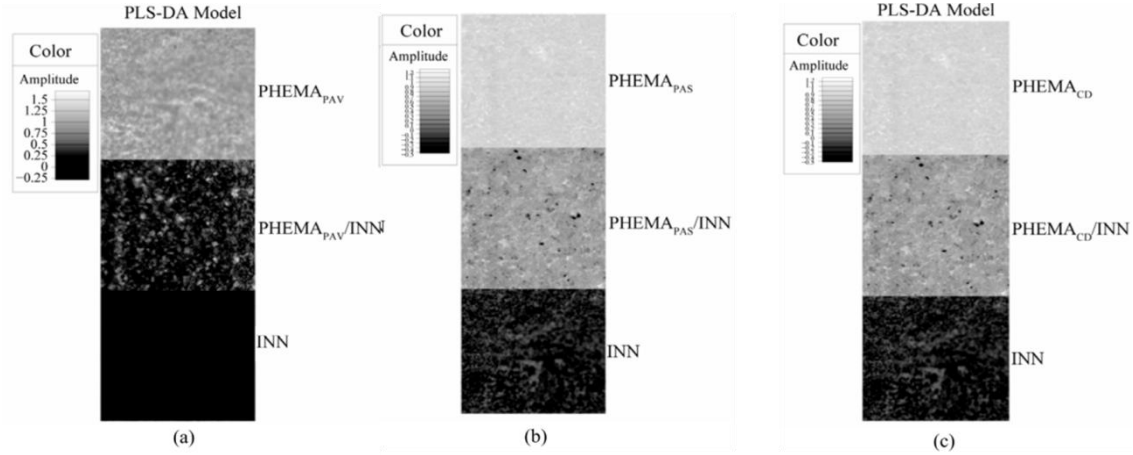

Figure 14 :Figure 14 shows the score images of indomethacin inclusion into polymer networks $PHEMA_{PVA}$ (a); $PHEMA_{PAS}$ (b); and $PHEMA_{CD}$. Image sourced from [4]. Level of grey depicts the distribution of the indomethacin in the synthesized polymeric matrices. Image sourced from [10]

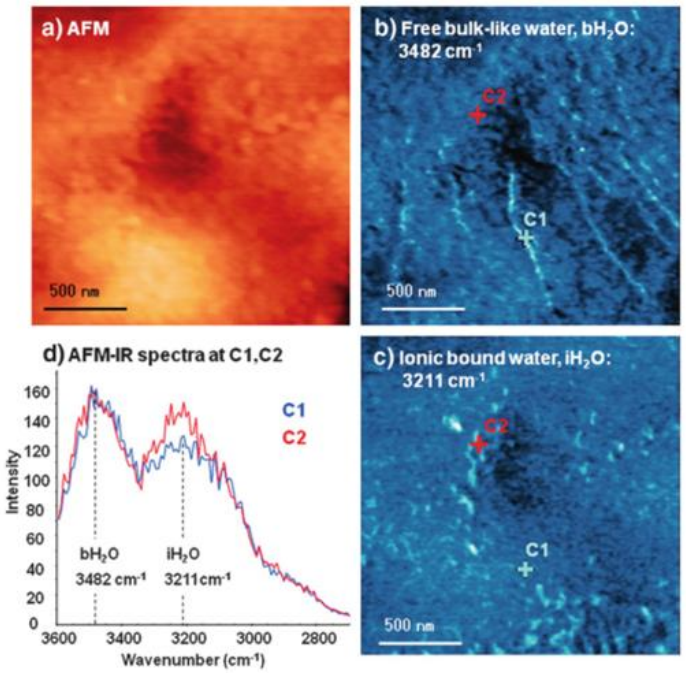

Figure 15 :AFM and AFM-IR chemical images of water within Nafion film, (a) AFM topography, (b) free water at 3482 cm−1 (c) bound water at 3211 cm−1, and (d) AFM-IR spectra at point C1 and C2. Images (a) and (b) show that free water and bound water are distributed differently on the Nafion membrane surface. Image sourced from [11]